Lübeck, Germany
12-13 July 2018

Proceedings of the

3rd KuVS/GI Expert Talk on Localization

ITG VDE

GI

Technische Universität Braunschweig

FACH HOCHSCHULE LÜBECK
University of Applied Sciences

u b
b UNIVERSITÄT BERN

HCU HafenCity Universität Hamburg

CoSA Center of Excellence

Editors: Marco Cimdins, Horst Hellbrück

Cover Picture: The cover was prepared by Marco Cimdins based on a photograph by Jens Thiedke.

Printed in Germany

https://doi.org/10.24355/dbbs.084-201807191218-1

Message from the Editors

Localization is a key technology in the field of medical, industrial and logistics applications, thus many applications will benefit from indoor localization. For instance, persons moving within an industrial security area are protected to enter a restricted area by triggering an alarm and shutting down hazardous machinery. In medical applications, emergency personnel is able to find injured persons much easier when the position is known. An application scenario in logistics is the localization of goods and equipment so that the flow of the production processes can be monitored and optimized. Although there is a huge research interest, there is no perfect solution for all the use cases in indoor localization scenarios. There is a variety of approaches and systems available by applying different technologies, e.g. optical, received signal strength, time of flight, etc. Each approach incorporates its own strengths and weaknesses.

The 3rd Expert Talk on Localization offers researchers a platform to discuss recent results of their work and share opinions with each other. This year's expert talk brings together researchers from academia and industry and offers a broad range of contributions in this challenging area including complete localization systems and demonstrations. The program covers ultra-wideband radio-based approaches, as well as received signal strength for indoor localization and the emerging field of machine learning and its application in localization.

We thank all authors for their contribution to the program. We express our appreciation to Lübeck University of Applied Sciences for its support, CoSA Center of Excellence for the organization of the meeting, HafenCity University, University of Braunschweig and University of Bern for their additional help as well as GI and KuVS for facilitating this event.

July 2018 M Cimdins & H Hellbrück

https://doi.org/10.24355/dbbs.084-201807191218-1

General Chair

Horst Hellbrück, Lübeck University of Applied Sciences

Organizing Committee

Eike Barnefske, HafenCity Universtiy
Mathias Pelka, Lübeck University of Applied Sciences
Yannic Schröder, University of Braunschweig
Zhongliang Zhao, University of Bern

Organisation

Marco Cimdins, Lübeck University of Applied Sciences

https://doi.org/10.24355/dbbs.084-201807191218-1

Table of Contents

Contributions

https://doi.org/10.24355/dbbs.084-201807191218-1

Lessons learned: Indoor Ultra-Wideband localization systems for an industrial IoT application

Swen Leugner* and Horst Hellbrück*†
*Lübeck University of Applied Sciences, Germany
Department of Electrical Engineering and Computer Science
Email: swen.leugner@fh-luebeck.de, hellbrueck@fh-luebeck.de
† University of Luebeck, Germany,
Institute of Telematics

***Abstract*—Since ultra-wideband (UWB) transceivers are available for wireless sensor networks, the usage in research and industry increased. Research efforts resulted in methods, measurement results, and solutions under laboratory conditions for a variety of indoor localization problems provided to the community. In this paper, we present an indoor positioning system (IPS) that is installed in a $1500\mathrm{m}^2$ real world production facility. In this real-world application, we faced some challenges that research has not addressed yet. For instance, challenges are receiving UWB signals from other floors in a multistory building through windows and multipath effects at walls like reflexions. We present solutions to increase the availability of such large-scale IPS, give a performance evaluation and recommendation for a modified NMEA sentence named iNMEA for IPS receivers.**

***Index Terms*—indoor positioning system, two-way-ranging, anchor, tag, multipath, ultra-wideband, indoor positioning testbed, increasing service availability**

I. Introduction

In recent years, interest in Indoor Positioning (IPS) is growing. Many scientific researchers and engineers in companies work on solutions for small area IPS; for instance, Schmitt et al. implemented [1] a reference system for indoor localization. The reference system is located on the university floor but limited to a corridor that has a length of approximately 100m. Their solution used a robot equipped with a camera system, which is not suitable for commercial indoor application due to privacy concerns. Tiemann et al. provided measurements from the ATLAS localization system [2]. The ATLAS localization system is based on the Time Difference of Arrival (TDoA) method. However, their experimental evaluation is performed in a small target area of less than $\mathbf{35m^2}$ without any obstacles in between. For our own evaluation, we installed an ultra-wideband IPS in a production facility, with the goal of tracking transport trolleys throughout the production process. Our IPS covers an area of $\mathbf{1500m^2}$. It is integrated into an industrial IoT application and to the best of our knowledge the largest of its kind in Germany. In this paper, we aim to share the experience and knowledge we gained throughout the planning, implementation, and installation of this large-scale IPS with the larger research community.

The paper is structured as follows: Section II provides an overview of the system design, components, and architecture. We describe our experience in Section III by presenting the challenges and solutions for large-scale localization systems. The paper concludes in Section IV with a short summary.

II. System Overview

In contrast to other research projects, we decided for a decentralized approach for implementation of the IPS. A decentralized approach means that the localization algorithm is executed on the IoT device, in our case a transport trolley, instead of the execution on a centralized localization server. Due to this decentralized approach, we benefit from shared resources and reduced complexity of the IPS. In Figure 1 we provide a system overview that illustrates the IPS and IoT application as well as the used technologies.

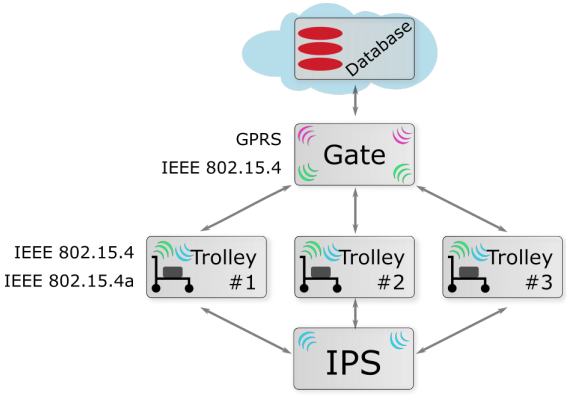

Fig. 1: Architecture of our industrial IoT application

The transport trolley utilizes two wireless sensor network standards: IEEE 802.15.4 and IEEE 802.15.4a. While the upper layers of the standards are similar, the main difference is the physical layer. IEEE 802.15.4 applies Offset-QPSK whereas IEEE 802.15.4a builds on ultra-wideband (UWB) technology. Because UWB signals are narrow in the time-domain, they are well-suited for measuring time of flight for IPS. For our indoor application, we deployed the well-known Decawave DW1000 UWB transceiver which measures timestamps with a resolution of 15.65 ps. The UWB transceiver performs localization whereas the IEEE 802.15.4 transceiver is used for the IoT communication. In our IoT application, the sensor node on the transport trolley wakes up every 5

https://doi.org/10.24355/dbbs.084-201807191218-1

TABLE I: Comparison of NMEA and iNMEA

Name in NMEA	Example	NMEA	iNMEA
Sentence ID	$GPGGA	GNSS Fix Data	IPS Data
Time	180834	18:20:11	Reserved for later use
Latitude	402.89, N	4d 2.89' N	x = 402.89 m
Longitude	81.76, W	8d 176' W	y = 81.76 m
Fix Quality {0,1,2}	1	0 - invalid 1 - GPS fix 2 - DGPS fix	0 - invalid 1 - 1st floor 2 - 2nd floor
Number of Satellites	04	4 Satellites in View	4 anchors used for result
HDOP	1.5	Horizontal accuracy	Reserved for later use
Altitude	370.0,M	370.0 Meters over ground	Encoded unique anchor IDs
Height of geoid	-14.0 M	-14.0 meters	Reserved for later use
Time since last DGPS update	103	Age of DGPS data	Time until position result [ms]
DGPS reference station id	200	Differential Station 200	Reserved for later use
Checksum	*13	Check for tx errors	Check for tx errors

minutes and initiates the localization process by switching on microcontroller board with the DW1000 transceiver. The sensor node shuts down the power supply of the microcontroller board after 10s independent of the status of the localization process. During the localization process, distances between anchor and the sensor node on the trolley are estimated by a two-way-ranging (TWR) algorithm. We apply the TriClock [3] algorithm to compensate for clock drift during the ranging. If the position is successfully calculated, the IPS microcontroller sends an iNMEA string via USART to the application microcontroller. The application microcontroller adds additional sensor data and transmits a frame to the IEEE 802.15.4 gateway. Finally, the gateway forwards the message to the database of a cloud service, see Figure 1.

A. iNMEA

We designed our IPS for easy and seamless integration into existing IoT platforms. Therefore, we deployed a derivate of NMEA 0183-HS protocol between the application and IPS microcontrollers on the transport trolley. NMEA 0183-HS is widely used in Global Navigation Satellite Systems (GNSS) and is commonly supported by IoT platforms. For our purpose, we adopted the Global Positioning System Fix Data (GPGGA) sentence code and named it Indoor NMEA (iNMEA) to account for our changes to the NMEA sentence. Table I compares the message fields of NMEA and iNMEA.

Our main modification to NMEA was changing the geographic coordinates used by GNSS to cartesian coordinates that are referenced to a fixed point in the area where the IPS is deployed. Secondarily, we included additional diagnostic data in the protocol. The *Time until Position* provides the time for localization. This time increases in situations where non-optimal anchor configurations were chosen, too few anchors can be reached or many collisions occured during media access. The *Encoded Anchor IDs* records the specific anchors that were used in the localization algorithm, which helps to diagnose wrong anchor positions and identify multipath propagation. Due to our positive experience, we recommend the iNMEA protocol for future highly integrated IPS services.

III. Challenges and Solutions

During deployment and tests some challenges occured that were not addressed by research and industry.

First, a significant difference compared to state of the art system and a challenge by itself is that the sensor node on the transport trolley regularly shuts down the IPS microcontroller for several minutes in our application. Hence, on every power up, the transport trolley could have moved in the production site and information about anchors e.g. might be completely outdated. We addressed the problem of finding anchors by sending periodic beacons by each anchor with a period of 1s. Each beacon includes the absolute position of the anchor in three dimensions and the anchor's unique identification number. When switched on, the IPS microcontroller on the transport trolley first listens for n seconds for beacons. After that, it starts ranging and calculates distance to each anchor.

Secondly, due to shadowing effects, the average range was 15m or less in the production facility. This is less than 40% of the typical communication range measured by others [4], [5]. The short communication range required many anchors that we had to install. In the end, we deployed 44 anchors to cover the target area. In a second step after evaluation of the system we solved the problem partially by increasing the transmission power level of the DW1000. However, this approach need careful consideration as raising the power results in a higher spectral emission in the communication channel. Such a solution might exceed regulatory limits, depending on the region.

Third, another issue with the increasing transmission power is that multipath effects occur more frequently. Indeed, by increasing the power, the DW1000 received beacons from anchors placed on other floors. We were able to filter out beacons originating from different floors in two steps. First, we added a floor identifier field to each beacon and utilized NMEA's fix quality to encode the floor level (see Table I). Then, we applied an algorithm that decided on the floor based on the received signal strength of beacons. We select the floor according to the strongest received beacon signal and ignored all anchors from other floors in the following. However, intra-floor multipath effects occured, i.e. ranging errors due to non-line-of-sight connections and signal reflection on the walls. To solve this problem, we used a new localization algorithm called mRansac [6].

Fourth, the last problem we had to solve were anchor geometries that produce erroneous results according to the topology of the anchors. In order to rate topologies we introduce a metric called horizontal dilution of precision (HDOP) that is calculated based on the anchor positions and the estimated position which is used to rate solution for the mRansac algorithm.

https://doi.org/10.24355/dbbs.084-201807191218-1

A. Performance Evaluation

In this subsection, we provide results of performance measurements collected with early and final software incl. configuration of the IPS. These performance measurements were collected with the help of our iNMEA protocol during the operation of the IPS in the production. A key performance indicator for localization is success rate of the localization process. In the first version in 2017 we reached 80% within a period of 28 days, see Figure 2. In our application we aim for a production optimization according to lean production philosophy, therefore the success rate needs to be close to 100%.

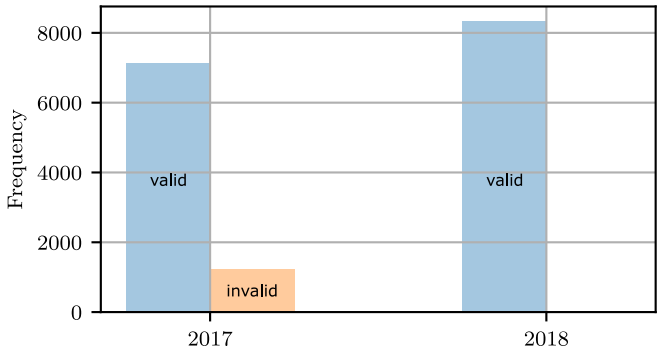

Fig. 2: Comparison of valid position flag of iNMEA in 2017 and 2018

Due to our efforts described in Section III, the success rate of our IPS service increased to 100%. In the version of 2017 quite often only beacons from 3 anchors were received, see Figure 3. 3 anchors are not always enough to calculate a valid position. If anchors are aligned in a line, the algorithm will not be able to calculate a valid position. In the version of 2018, in most cases we reached more than 10 anchors and therefore had a variety of selection of anchors to find a valid position.

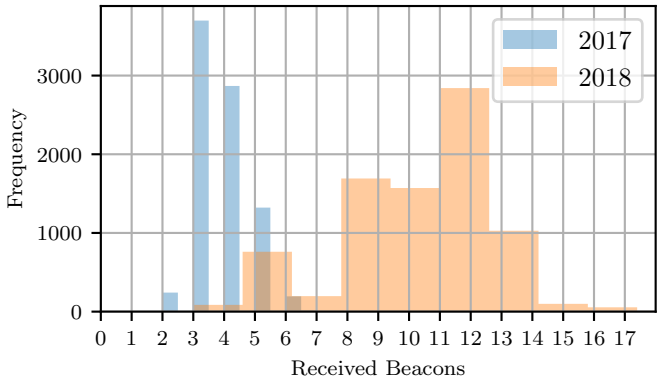

Fig. 3: Number of received Beacons

IV. Conclusion

In this paper, we showed that a large-scale indoor positioning system provides a variety of challenges. We identified effects for large-scale and real-world deployments which are not accounted for in existing work e.g. multipath propagation. We drew attention to balance UWB communication range for a reasonable number of anchors and to avoid multipath. Additionally, we recommended the use of iNMEA as a communication protocol between the IPS and application microcontrollers. Finally, we showed how to increase the availability of an IPS service in large-scale positioning systems.

Acknowledgments

This publication is a result of the research work of the Center of Excellence CoSA in project DRAISE which is funded by the German Federal Ministry of Education and Research (BMBF), FKZ 16KIS0430. Horst Hellbrück is adjunct professor at the Institute of Telematics of the University of Lübeck.

References

[1] S. Schmitt, H. Will, B. Aschenbrenner, T. Hillebrandt, and M. Kyas, "A reference system for indoor localization testbeds," in *Indoor Positioning and Indoor Navigation (IPIN), 2012 International Conference on*. IEEE, 2012, pp. 1–8.

[2] J. Tiemann, F. Eckermann, and C. Wietfeld, "Atlas-an open-source tdoa-based ultra-wideband localization system," in *Indoor Positioning and Indoor Navigation (IPIN), 2016 International Conference on*. IEEE, 2016, pp. 1–6.

[3] S. Leugner, M. Constapel, and H. Hellbrück, "TriClock Clock Synchronization compensating Drift, Offset and Propagation Delay," in *IEEE International Conference on Communications*. IEEE, 2018.

[4] V. Barral, P. Surez-Casal, C. J. Escudero, and J. Garca-Naya, "Assessment of uwb ranging bias in multipath environments," in *International Conference on Indoor Positioning and Indoor Navigation (IPIN), Alcala de Henares, Spain*, 2016.

[5] A. R. J. Ruiz and F. S. Granja, "Comparing ubisense, bespoon, and decawave uwb location systems: indoor performance analysis," *IEEE Transactions on instrumentation and Measurement*, vol. 66, no. 8, pp. 2106–2117, 2017.

[6] M. Pelka, P. Bartmann, S. Leugner, and H. Hellbrück, "Minimizing Indoor Localization Errors for Non-Line-of-Sight Propagation," in *International Conference on Localization and GNSS*, 2018.

https://doi.org/10.24355/dbbs.084-201807191218-1

CONCEPT FOR REAL-TIME LOCALIZATION BASED ON SMARTPHONE CAMERA AND IMU

Janek Stoeck, Harald Sternberg
Dept. Geodesy and Geoinformatics
HafenCity University Hamburg
Hamburg, Germany
firstname.name@hcu-hamburg.de

***Abstract*—This paper introduces a concept for a real-time localization system based on sensors available on smartphones. The proposed method relies on inertial measuring units, on one or more cameras and a given floor plan. Each of the used sensor produces position and orientation (pose) which will be fused with a kalman filter to get the best possible result. 3D point clouds generated from images of the camera are used to derive partly floor plans. By comparing the result to a given map the scaling and positioning fixes are adopted.**
Different possible platforms, like standard smartphones with one or smartphones with more than one camera, can be used to realize this concept. First experiments were done in two different approaches (with inertial and visual navigation) in order to get an idea what accuracies are achievable. The concept will be implemented and tested on a Samsung Galaxy S8.

***Index Terms*—indoor navigation, visual inertial navigation, smartphone, position estimation**

I. Introduction

Since 2011 the HafenCity University Hamburg (HCU) investigates smartphone sensors in context of indoor navigation. The utilization of smartphones for navigation, usually with the global navigation satellite system (GNSS) principle, is wide spread and commonly known, and the implemented sensors are a good base for developing an indoor navigation system. While GNSS is only available in outdoor environments, other solutions for the indoor environment has to be found. The purpose of this paper is to introduce a concept for indoor localization based on inertial and visual sensors, while the focus of this concept lies on the camera system.

II. Related Work

Nowadays cameras are well known for the purpose of visual odometry for robots, but they are also used in some pedestrian navigation systems. [1] and [2] using feature matching algorithms to determine the camera pose. [1] use a video stream to identify known key points, which are geo-referenced before, and inertial sensors. They propose a method of two phases: The first phase is an offline phase, where distinctive points (anchors) in the building are geo-referenced and processed with the Speeded Up Robust Features (SURF) algorithm, to construct a databese of reference images with known coordinates. In the second (online) phase, a smartphone's camera is used to take query pictures of these anchors, which will be send to a server to do a feature matching with the database images. The best fit is then used to fix the position, which is estimated by dead reckoning (DR) with step counter and heading of a magnetometer.
[2] propose a method to estimate a position using GNSS, inertial measuring unit (IMU) and the smartphone camera. The orientation is a solution of a bundle block adjustment with the input of all available sensor data.
Both of these methods use geo-referencing, either in runtime or before the online phase. The geo-referencing in an offline phase is a step, that may be done once, but it is time consuming and in the case of [1] heavily depends on the database. Furthermore, it requires a connection to some kind of server. The work of [2] depends on GNSS and as already mentioned this principle is not suitable for indoor navigation.
[3] developed a fusion algorithm for indoor navigation which uses inertial data and topological information to achieve an accuracy of less than 5 m in 70 %. His work is an inspiration for the following proposed method, because some parts of this work (like the step counter) are adopted from it. Further no external infrastructure is required and it is also developed and tested at the HCU.

III. Concept

The development of the following proposed concept aims to create a system, which is meant for indoor navigation and only relies on smartphone sensors. The developed algorithms should be executed in runtime on the smartphone. The first step is to initialize a start position. The navigation is realized by a DR based on IMU data and by image based navigation. Both approaches support each other in different ways. A given map of the building and a routing graph trough it are prerequisites for this method.

A. Proposed Method

Our proposed method can be split into two different modules, "inertial" and "visual" sensing. Fig. 1 shows the principle of the inertial sensing, which is realized by accelerometer, gyroscope and barometer. The accelerometer is used to implement a step counter like in [3]. The step counter is based on the accelerometer z-axis and has two conditions to be fulfilled. First, an initial maximal threshold has to be passed followed by passing the lower threshold. If these conditions are true, a step is detected. If the actual

https://doi.org/10.24355/dbbs.084-201807191218-1

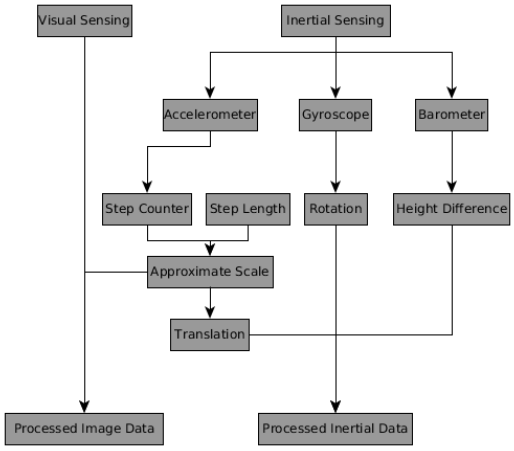

Fig. 1: Detailed step of inertial Sensing

accelerometer z-reading passes the thresholds value including a scaling factor, the threshold value increases to the actual z-reading. This is the advantage of this step counter, because it ensures, that it adopts the walking behavior of the user. In our proposed method, the step also serves as a scale for the visual sensing. Together with the integrated gyroscope readings, DR can be performed. The formula can be seen in (1), where $\vec{x}_i$ is the actual position, $\vec{x}_{i-1}$ is the previous position and R and t are the rotation and translation between both. The principle of the step counter can be seen in Fig. 2.

$$\vec{x}_i = \vec{x}_{i-1} + R * t \tag{1}$$

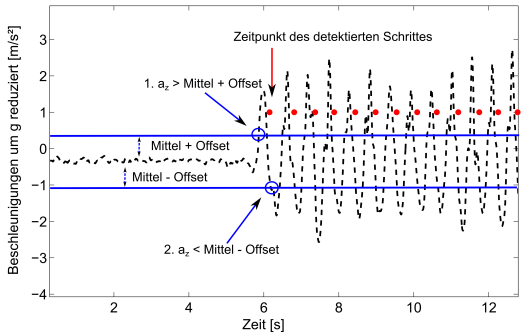

Fig. 2: Principle of the step counter. Black line = accelerometer z-axis reduced by g, blue line = minimal and maximal threshold to detect a step, red dot = detected step [3]

The algorithm in [3] also takes the routing graph with a particle filter into account. The inertial sensing of our method does not require a filter, because the routing graph acts as a line of orientation. If the user navigates near the routing graph and the heading of the smartphone and graph are nearly the same, the position estimated by DR is snapped to the graph and the orientation value is set to the heading of the graph. If the heading is not the same, the algorithm is able to leave the graph, to ensure that the device is able to recognize a trajectory off-sided the graph.

The visual sensing is realized by processing images of the smartphone camera and can be seen in Fig: 3. The principle to get the camera pose is based on feature matching. To ensure that the data obtained from the visual sensing and the inertial sensing are synchronized, the step counter serves as a trigger. Additionally this has the effect, that the translation of the IMU and the visual sensing are equal and the step length can be taken as a scale for the image processing, so there is no need of geo-referencing any anchors.

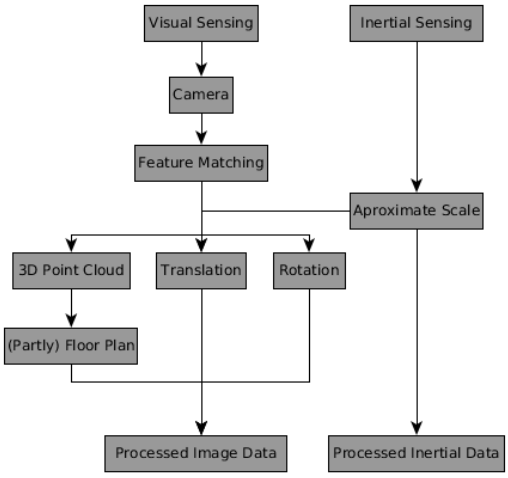

Fig. 3: Detailed step of visual Sensing

Furthermore, the image data is used to obtain 3D point clouds, from which a partly floor plan can be derived. As this system has the aim to serve as an indoor navigation system, there is a given map of the surrounding environment. Both maps can be compared and the scale of the visual translation and the pose of the smartphone can be corrected. This is achieved by a best fit transformation. The pose of the DR can be taken as an approximation for the area of interest, so the computation resources are not used to capacity.

In the current stage of development the visual sensing is realized in post processing, where the images are processed with SURF to find correspondences, which are used to estimate the fundamental matrix and epipolar inliers. With these and the calibration values of the camera a relative camera pose can be detected. To bring the concept onto the smartphone the open source library OpenCV will be used.

Both poses of the modules are going to be fused with a simple kalman filter, to get a more reliable and robust solution. It is assumed that the orientation of the camera is more accurate than the orientation of the IMU, but the translation relies on a scale which is set to the step length. Because of this, the kalman filter weights the orientation of the camera higher than the IMU and the translation are weighted equally.

https://doi.org/10.24355/dbbs.084-201807191218-1

B. Used Hardware

A Samsung Galaxy S8 is used to realize this concept. The specifications are shown in Table I. The phones IMU components range can be set in different areas, but it is assumed that the lowest area ($\pm$ 2 g & $\pm$ 125 $\frac{°}{s}$) are sufficient, as a normal walking behavior should not exceed these values. This smartphone is a good choice because it represents the most spread kind of phone, regarding the camera setup. There are other options like phones that have more cameras to create a depth field, but most of the manufacturers do not provide a library to implement the depth cameras into an own application.

TABLE I: Samsung Galaxy S8 - Specifications [4]

IMU - STMicroelectronics LSM6DSL	
Acc. range	$\pm$ 2 g .. $\pm$ 16 g
Acc. sensivity	0.061 .. 0.488
Angular rate range	$\pm$ 125 $\frac{°}{s}$.. $\pm$ 2000 $\frac{°}{s}$
Angular rate sensivity	4.375 .. 70
Camera - Sony IMX333	
Sensor size	1/2.55 ”
Pixel size	1.4 µm
Resolution	up to 12 MP
FOV	77°
Aperture	F1.7

IV. Experimental Results

A. Inertial Sensing

A test route has been followed and can be seen in Fig. 4. The trajectory starts and ends at the same position. The smartphone was held in a 45° angle in relation to the ground. Table II shows the position estimation of the inertial sensing and has a closure error of 1.83 m. The algorithm recognized 412 steps. These results show that the step counter and the support through the routing graph as an update for position and orientation work quite well.

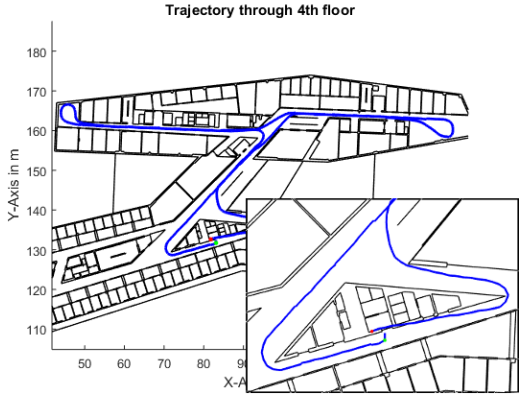

Fig. 4: Trajectory through 4th floor of the HCU building

TABLE II: Results of inertial trajectory

	X [m]	Y [m]
Start	83.100	131.700
End	81.450	132.500
Abs. difference	1.650	0.800
Dist. of closure error	1.830	

B. Visual Sensing

The investigations to prove the visual sensing concept were done in post processing as this module is not implemented on the smartphone yet. They should demonstrate which results are achievable when utilizing smartphone cameras.

1) Trajectory: The visual sensing was tested in its capability to follow the pose along a straight line. The phone was fastened on the sledge of a comparator track and was moved in equal distances along the track. These distances were 0.75 m, as this is assumed by [5] to be the step length for the most people. The step is taken as scale for the processing. The smartphone camera was used to capture a video stream with 1280x720 px. At each position to be processed a sound indicator indicates the time which frame should be taken. The images were processed with the SURF algorithm to get the translation and rotation of the camera, which were used to perform DR.
The results are shown in Table III. It should be noticed that the first position is 0.30 m. The means of the values show that the visual sensing is capable to follow a straight line with an error less than 2 cm.
The processing was repeated 20 times to verify the results are

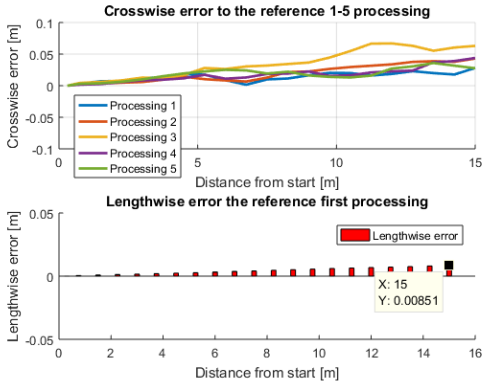

Fig. 5: Length- and crosswise error along a reference

equal. As seen in Fig. 5, where the crosswise error of the first five processing repetitions are pictured, the errors show similar behavior. They drift to the left. It seems that the feature points to the left are weighted more than to the right. This is because the right side to the comparator track is a gray wall with low contrast, and the right side has many different objects in it. They are not exactly equal, because the different processing repetitions have not found the same features. The lengthwise

https://doi.org/10.24355/dbbs.084-201807191218-1

error shows a smaller value and it has a constant inclination. This is because the small errors are accumulated.

TABLE III: Results of visual made trajectory compared to a straight line

Distance [m]	δx [m]	δy [m]	δz [m]	δ [m]
0.30	0.000	0.000	0.000	0.000
0.75	0.003	0.002	0.000	0.004
1.50	0.007	0.002	0.001	0.007
...	...	...	...	...
13.50	0.020	-0.008	0.007	0.023
14.25	0.018	-0.010	0.008	0.022
15.00	0.028	-0.007	0.008	0.030
Mean	0.001	0.005	0.005	0.012

2) Point cloud: The same images were used to derive point clouds from them. A reference point cloud was received by a laserscan. The images were processed with the software PhotoScan from Agisoft. As seen in Fig. 6 gaps in the point cloud occurred due to the fastening of the phone in portrait mode. This is why more of the ceiling was captured than the wall next to the comparator track. Fig. 6 also shows the differences between the reference and the derived point cloud. Points with a low difference are colored blue, while points with a difference up to 0.15cm are colored red.
Fig. 7 shows the allocation of the points into eight classes. The

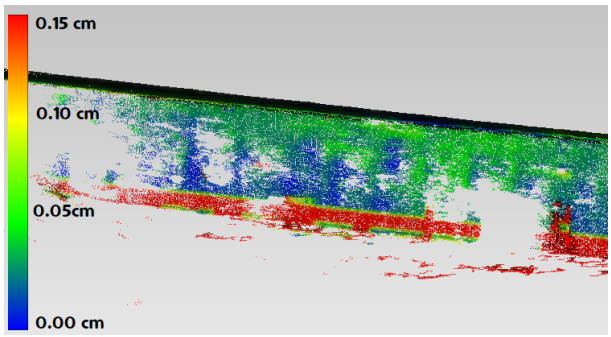

Fig. 6: Differences between the point clouds from images and from laserscanning

intervals of the classes and the number of points as percentage are shown in Table IV. More than 60 % of the points have a lower difference to the reference than 5.6 cm which is a suitable result, regarding to the unstable camera parameters of smartphones.

V. Conclusion and Outlook

This paper presents a concept for a visual inertial indoor navigation system. This concept is based on a smartphone IMU and camera. In addition to the achieved translation and rotation trough the camera, the images can be used to derive 3D point clouds. These can be used to get partly floor plans, which can be compared to a given map to achieve pose and scaling corrections.
First tests show, that each module on its own is able to achieve good results. Especially for the visual sensing more

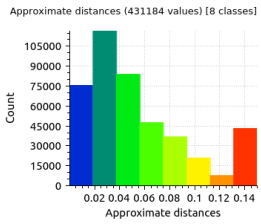

Fig. 7: Histogram of the differences

TABLE IV: Statistics of the histogram

Class	Start [m]	End[m]	[%]
1	0.000	0.019	17.490
2	0.019	0.038	26.999
3	0.038	0.056	19.433
4	0.056	0.075	10.992
5	0.075	0.094	8.517
6	0.094	0.113	4.826
7	0.113	0.131	1.750
8	0.131	0.150	9.993

tests with longer distances and with rotations have to be done. The executed tests are also under optimal conditions, with no rolling shutter effects, which are assumed to be seen in real life conditions. The visual sensing has to be tested while walking with the device in the hand.
While the inertial sensing module is already implemented on a smartphone, the visual sensing is not. The next steps are to implement the visual sensing in a way that both modules can run independently on a smartphone. Furthermore both module data should be combined with a kalman filter to eliminate the weaknesses of each module.
As mentioned before, there are other camera setups available in smartphones and a very interesting device is the Lenovo Phab 2 Pro, as it has an infrared projector available and allows direct measurements of depths. In this way the scaling problem can be solved.

References

[1] L. Atzori, T. Dessi, and V. Popescu, "Indoor navigation system using image and sensor data processing on a smartphone," in *Optimization of Electrical and Electronic Equipment (OPTIM), 2012 13th International Conference on*. IEEE, 2012, pp. 1158–1163.
[2] M. Piras, A. Lingua, P. Dabove, and I. Aicardi, "Indoor navigation using smartphone technology: A future challenge or an actual possibility?" in *Position, Location and Navigation Symposium-PLANS 2014, 2014 IEEE/ION*. IEEE, 2014, pp. 1343–1352.
[3] T. Willemsen, "Fusionsalgorithmus zur autonomen positionsschätzung im gebäude, basierend auf mems-inertialsensoren im smartphone," Ph.D. dissertation, HafenCity University Hamburg, 2016.
[4] Samsung. (2018) Specifications. [Online]. Available: https://www.samsung.com/global/galaxy/galaxy-s8/specs/ [Accessed: 28- Jul- 2018]
[5] J. Kupke, T. Willemsen, F. Keller, and H. Sternberg, "Development of a step counter based on artificial neural networks," *Journal of Location Based Services*, vol. 10, no. 3, pp. 161–177, 2016.

https://doi.org/10.24355/dbbs.084-201807191218-1

Demo: InPhase – No-Cost Phase-based Ranging and Localization in Wireless Sensor Networks

Yannic Schröder, Dennis Reimers and Lars Wolf
Institute of Operating Systems and Computer Networks
Technische Universität Braunschweig
Braunschweig, Germany
Email: [schroeder|dreimers|wolf]@ibr.cs.tu-bs.de

***Abstract*—The InPhase system demonstrates phase-based ranging and localization in Wireless Sensor Networks. Our wireless sensor nodes are equipped with an off-the-shelf IEEE 802.15.4 radio transceiver with integrated Phase Measurement Unit. The Active-Reflector-Principle allows to establish a meaningful distance in meters between two sensor nodes. Based on such distance measurements, we demonstrate real-time 3D localization of a sensor node in a Wireless Sensor Network by employing a particle filter. InPhase generates distance and location information at no additional hardware cost and implements all functionality in software.**

I. Introduction

Physical distance between nodes and location information can be valuable additions to the capabilities of a Wireless Sensor Network (WSN), especially if they come at no extra cost. InPhase allows to measure distances between Commercial Off-The-Shelf (COTS) radio transceivers with built-in Phase Measurement Units (PMUs) by measuring the phase angle of a Continuous Wave (CW) radio signal. [1], [2]

We demonstrate localization by using Atmel AT86RF233 IEEE 802.15.4 transceivers in the 2.4 GHz frequency band [3]. By employing the Active-Reflector-Principle (AR-Principle) the physical distance between sensor nodes can be measured [4]. A sensor node with unknown location (tag) measures multiple distances to nodes with known location (anchors) and reports those to a computer running the localization algorithm. A particle filter solves the localization problem based on the reported distances and the anchors' locations.

II. Related Work

The Atmel Ranging Toolbox (RTB) uses the AR-Principle with the PMU of an AT86RF233 radio transceiver [5]. However, as shown in [1], InPhase outperforms the RTB in terms of accuracy. Further, as the RTB firmware is only available as binary distribution for Atmel microcontrollers, it cannot be easily integrated with other wireless sensor hardware.

The crucial part of computing distance values from phase ranging data is the reconstruction of the slope of the measured sawtooth signal. Pelka et al. propose a method to extract the slope of the phase directly [6].

However, Gunia et al. found that the approach from Pelka et al. results in larger distance errors with increased measurement distance. Instead, they propose to use our distance estimation via autocorrelation and Fast Fourier Transformation (FFT). [7]

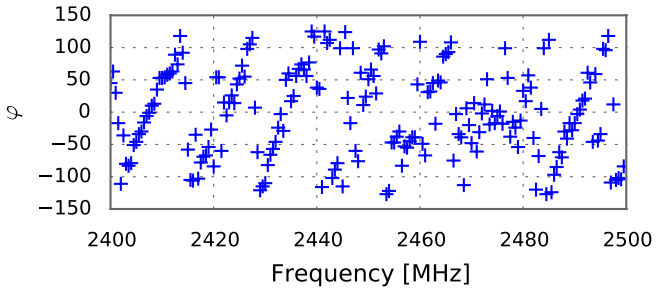

Figure 1. Raw phase response measurement (reproduced from [1])

Oshiga et al. propose a hybrid approach between the direct reconstruction from Pelka et al. and our distance estimation via FFT. A measured sawtooth signal is stacked on top of itself and a linear function is computed that fits the measurement data best. The sawtooth signal does not need to be unrolled which is error-prone for noisy data. The output of the algorithm resembles the output of our FFT and the distance is estimated similarly by search for the maximum peak in the output data. Furthermore, they propose to use multiple peaks from the result data for localization. Non-Line-of-Sight (NLOS) conditions lead to result data where the exact location cannot be determined. By passing multiple possible distances to the localization stage, the localization algorithm might still be able to localize a node. [8]

We have improved our distance estimation algorithm by interpreting the measured phase angles as a complex signal in the frequency domain. Our evaluation shows, that the new algorithm outperforms our old version and the algorithm by Oshiga et al. Further, we found that the FFT resolution can be reduced when the result is interpolated without harming accuracy and precision. [2]

III. Phase-based Ranging

InPhase exploits the AR-Principle to measure distances between sensor nodes in a WSN. The AR-Principle allows to measure a phase angle of a CW radio signal without synchronized reference clocks at the sender and receiver. One node, the initiator, starts a measurement by sending a message to a second node, the (active) reflector. When both nodes agreed on the measurement parameters, a measurement of a signal's phase angle is executed over a spectrum of multiple frequencies. Figure 1 shows a resulting sawtooth signal. The

https://doi.org/10.24355/dbbs.084-201807191218-1

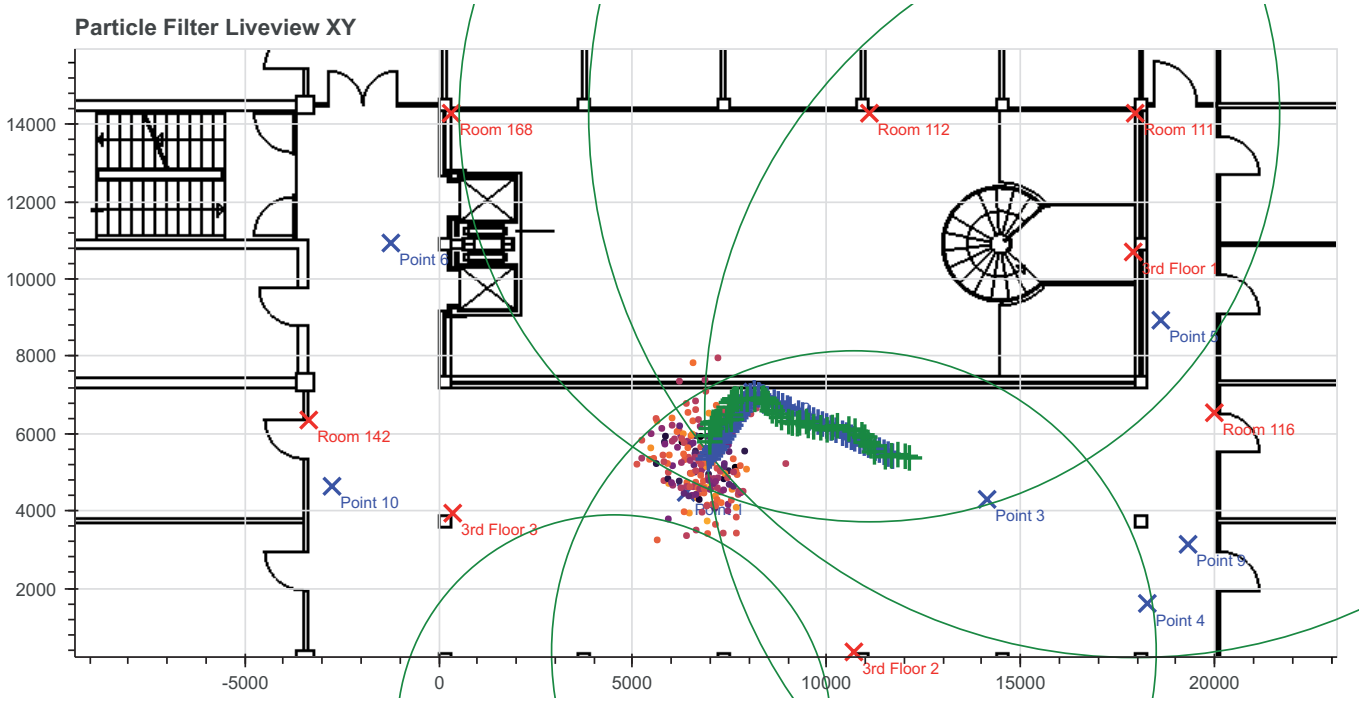

Figure 2. Visualization of the localization algorithm. Red x's: Anchor nodes. Blue x's: Known reference points. Green Circles: Measured distances. Blue +-symbols: Ground truth path. Green +-symbols: Localization output. Orange point cloud: Particles. Both axes are marked in millimeters.

Figure 3. Battery-powered InPhase sensor node.

steepness of the slope is proportional to the distance between both nodes. The distance can be computed via our algorithms presented in [1] and [2].

The new algorithm [2] allows to measure distances up to 300 m. However, as the maximum transmission range of wireless sensor nodes is restricted by the allowed maximum output power, this distance is not achieved in practice. We were able to measure distances up to 275 m with our hardware.

IV. Localization

To localize a sensor node, distances to sensor nodes (anchors) in known reference locations are measured. The sensor node to be localized (tag) initiates distance measurements with all anchors in a round-robin fashion and reports the measurements to an attached computer.

In the next step, distances from the obtained measurements are computed and consumed by a particle filter to localize the tag in 3D space. The particle filter has prior knowledge of the system via the positions of the particles from the last round and reports 3D coordinates. Each new measurement updates the location estimation by re-evaluating the particle positions and their likelihood to be in the correct location.

Figure 2 shows the output visualization of the system. In the background, a 2D map of the area is shown. The positions of reference anchors are marked with red x's and known ground truth locations are marked with blue x's. The particle cloud is displayed as a scatter plot of filled circles. The different colors indicate the probability of that particle. Lighter colors indicate higher probability. The green circles indicate the measured distances around the anchors. Blue +-symbols indicate the ground truth path that was taken, while green +-symbols indicate the reported location. Both of these plots have a short trace of previous positions to indicate the path that was taken.

V. InPhase Sensor Node

Our own battery-powered wireless sensor node is used for the demonstration, see Figure 3. It is based on the INGA wireless sensor node [9] and uses an ATmega1284p microcontroller [10]. The AT86RF233 radio is mounted on an extra

https://doi.org/10.24355/dbbs.084-201807191218-1

Figure 4. Panoramic view of the evaluation area of the Microsoft Indoor Localization Competition 2018.

circuit board to allow different experimental setups with other radio chips. The radio board features an SMA connector for experiments with different antenna designs.

Although we use our own modular sensor node, it does not feature any special hardware. Thus, InPhase remains a solution that requires only additional software on a sensor node and no extra hardware.

VI. Real-world Setup and Evaluation

The InPhase system competed in the Microsoft Indoor Localization Competition 2018 [11]. We deployed a total of 10 anchors on two floors and a large staircase. Figure 4 gives an impression of the evaluation area. For the evaluation, the tag was mounted to a LIDAR scanner which was used to obtain ground truth measurements [12]. During evaluation, a person walked along a previously secret path through the whole area. Our system scored an average location error of 0.99 m.

The biggest challenge is obtaining the ground truth locations of anchor nodes in the local coordinate system. Especially in buildings with complex architectural features like columns and sloping walls, it is hardly possible to obtain measurements with a laser rangefinder. One team used a total station for ground truth measurements. This resulted in very precise reference anchor locations for their setup.

VII. Demo Setup

Multiple anchor nodes are mounted to the walls and preferably to the ceiling of the demonstration area. The ground truth location of these nodes will be measured. The duration of the offline survey is dependent on the number of tags and the complexity of the setup area. The tag node is mounted on top of a camera tripod and can be freely moved to different locations. A single-board computer relays the measurements from the tag node to a computer that runs the localization algorithm and displays the results as well as the current state of the particle filter in real-time, see Figure 2.

References

[1] G. von Zengen, Y. Schröder, S. Rottmann, F. Büsching, and L. C. Wolf, "No-Cost distance estimation using standard WSN radios," in *The 35th Annual IEEE International Conference on Computer Communications (INFOCOM 2016)*, San Francisco, USA, Apr. 2016.

[2] Y. Schröder, D. Reimers, and L. Wolf, "Accurate and precise distance estimation from phase-based ranging data," in *2018 International Conference on Indoor Positioning and Indoor Navigation (IPIN)*, Sep. 2018.

[3] *Low Power, 2.4GHz Transceiver for ZigBee, RF4CE, IEEE 802.15.4, 6LoWPAN, and ISM Applications*, Atmel Corporation, San Jose, Jul. 2014.

[4] W. Kluge and E. Sachse, "System, method, and circuit for distance measurement between two nodes of a radio network," Feb. 2014, US Patent 8,644,768.

[5] *Atmel AVR2150: RTB Evaluation Application – User's Guide*, Atmel Corporation, San Jose, Feb. 2013.

[6] M. Pelka, C. Bollmeyer, and H. Hellbrück, "Accurate radio distance estimation by phase measurements with multiple frequencies," in *2014 International Conference on Indoor Positioning and Indoor Navigation (IPIN)*, Oct 2014, pp. 142–151.

[7] M. Gunia, A. Zinke, N. Joram, and F. Ellinger, "Setting up a phase-based positioning system using off-the-shelf components," in *2017 14th Workshop on Positioning, Navigation and Communications (WPNC)*, Oct 2017.

[8] O. Oshiga, A. Ghods, S. Severi, and G. Abreu, "Efficient slope sampling ranging and trilateration techniques for wireless localization," in *12th Workshop on Positioning, Navigation and Communication*, Mar. 2015.

[9] F. Büsching, U. Kulau, and L. Wolf, "Architecture and evaluation of INGA - an inexpensive node for general applications," in *Sensors, 2012 IEEE*. Taipei, Taiwan: IEEE, Oct. 2012, pp. 842–845.

[10] *8-bit Atmel Microcontroller with 16/32/64/128K Bytes In-System Programmable Flash*, Atmel Corporation, San Jose, Jan. 2015.

[11] D. Lymberopoulos, J. Liu, V. Sequeira, V. Jain, N. Trigoni, A. Rowe, and N. Moayeri, "Microsoft Indoor Localization Competition - IPSN 2018," Apr. 2018.

[12] C. Belenguer, P. Taddei, S. Ceriani, E. Wolfart, and V. Sequeira, "Localization and tracking in known large environments using portable real-time 3d sensors," in *Computer Vision and Image Understanding*, vol. 149, Aug. 2016, pp. 197–208.

https://doi.org/10.24355/dbbs.084-201807191218-1

https://doi.org/10.24355/dbbs.084-201807191218-1

Anchor Pair Selection in Unilateral TDoA Localization Topologies

Reza Zandian, Ulf Witkowski
Department of Circuits Design and Electronics
South Westphalia University of Applied Science
Soest, Germany
Email: {zandian.reza, witkowski}@fh-swf.de

***Abstract*— This paper addresses the pair selection problem of the unilateral time difference of arrival (TDoA) localization method. Two common concepts of pair selection are star form which uses a unique reference node for pairing all nodes and the chain form which links each node to its next available node. The problem of the star form is the possibility of occurring non-line of sight (NLOS) conditions between some anchors. The chain form has an issue with increasing variance of the noise as the number of anchors increases. A new hybrid form is proposed which avoids NLOS conditions and at the same time pertains the amount of noise at its minimum possible. Practical results confirm the superior performance of the proposed approach.**

***Keywords*— Localization, TDoA, UWB, Unilateral**

I. INTRODUCTION

Among the localization approaches proposed so far, the time-based methods promise better accuracy and reliability in noisy and challenging conditions of the indoor environment. This is especially the case, when the ultra-wideband (UWB) localization systems are applied. UWB offers higher accuracy compared to other radio-based technologies due to its less sensitivity to multipath effect as a result of their large utilized bandwidth [1]. Possible connection topologies of time-based approaches are time of arrival (ToA) which extracts the range information from communications between only two nodes and time difference of arrival (TDoA) which performs the ranging between two anchors and one node. The TDoA approach is the main choice of designers when large number of nodes are involved in the network [2]. This is mainly due to the several features of this technique which are less signal interference, simplicity of the implementation, lower radio traffic, lower power consumption of the nodes and higher location update rate even though larger number of the nodes compared to ToA approach are involved [3].

The TDoA technique can be implemented in two different constellations [4, p. 192]. The first one is called unilateral in that the anchor nodes are transmitter and the mobile nodes are receiver. This constellation is useful for navigation and self-localization applications where the location data is required in the mobile node itself. The other constellation is multi-lateral in that the anchors are receiver and the mobile nodes are transmitter. This technique is more suitable for tracking and monitoring applications where the location data is collected in a central server [3]. The unilateral technique needs to manage a time delay between the transmission times of the anchors to avoid signal interference. This is achieved by defining a reference node which triggers the transmission and dictates the timing in the network. The unilateral approach does not require clock synchronization between the nodes, however, a clock drift management algorithm is required to equalize the clock paces of all the nodes [5].

One major issue in the design process of the unilateral TDoA method is the criteria used for anchor pair selection. In terms of location of the anchors, many solutions are proposed in the literature [6, p. 61] but the pair selection criteria has not been addressed so far. This paper, introduces two common methods of pair selection in unilateral TDoA approach as star form and chain form based on UWB devices. The details and properties of each form are discussed and a new pairing style is proposed as hybrid form which combines the two previously introduced options for the sake of improving the localization performance.

II. UNILATERAL TDOA TOPOLOGY

The TDoA localization technique estimates the location of a node using trilateration method. In this case, the time difference of signal arrival in the mobile node is measured which can be represented as a hyperbola line between the two nodes. The location of the mobile node is estimated by calculating the intersection point of the hyperbolas for all involved anchor nodes. This concept is shown in Fig. 1.

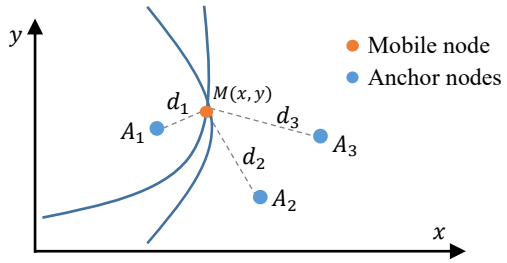

Fig. 1. Location estimation in the TDoA topology based on the intersection point of all hyperbolas

As mentioned before, anchor transmissions are performed sequentially with a certain time delay between transmissions. The transmission time of each anchor is calculated as:

$$t_{A_i tx} = t_{ref} + (i-1)t_{int}\,, \quad i = 2, \dots, n \tag{1}$$

where t_{ref} is the time that the reference node has transmitted a signal, t_{int} is a fixed time interval between two sequential

https://doi.org/10.24355/dbbs.084-201807191218-1

transmissions and i indicates the index of the transmitting anchor. The differential time of arrival in the mobile node is the interval delay subtracted from the difference of the received time from the two anchors. This can be presented in general form as:

$$T_{i,j} = t_{A_j rx} - t_{A_i rx} - (i-j)t_{int} \ , \ i \neq j \tag{2}$$

where $T_{i,j}$ is the differential time between the node i and j where $i > j$, parameter $t_{A_j rx}$ is the signal arrival time of the anchor j at the mobile node and t_{int} is the interval delay.

III. Anchor Pair Selection Concepts

In a localization system with many anchors, a concept is required to define which anchors should be paired in order to extract the differential time. A very common concept is to define the first anchor as reference and pair all the anchors with this anchor node. We call this pairing concept as star form. The connection structure of the star form for four anchors is demonstrated in Fig. 2.a.

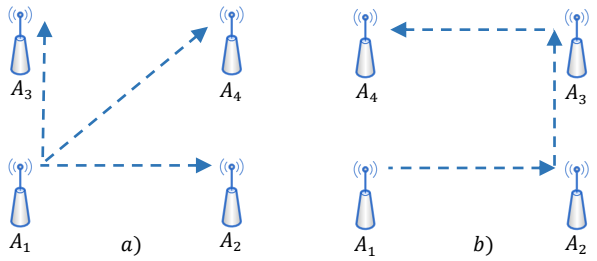

Fig. 2. a) Star form pairing concept of the anchors with anchor 1 as reference, b) Chain form of anchor pairing with linking anchors on the perimeter

The advantage of the star form is that, in all the anchors, same level of measurement noise can be observed as they are compared to a unique reference node. The next transmission time of the anchor n in the star form including the noise term w can be calculated using:

$$t_{A_n tx} = t_{ref} + (n-1)t_{int} + w_n \tag{3}$$

Applying this equation in (2), we can deduct the new term:

$$T_{i,1} = t_{A_1 rx} - t_{A_i rx} - (i-1)t_{int} + w_i' - w_1' \ , \quad i = 2, \dots, n \tag{4}$$

where parameter w_i' is the sum of the transmission noise in anchor i and the measurement noise in mobile node. In order to define a metric for the variance, the expectation value of the noise term should be calculated according to:

$$Q = E\left[\left(T_{i,1} - E(T_{i,1})\right)\left(T_{i,1} - E(T_{i,1})\right)^T\right] \ , \ i = 2, \dots, n \tag{5}$$

The solution of this equation leads to development of a covariance matrix with diagonal elements defined as:

$$Q = E[(w_i' - w_1')^2] = E[w_i'^2] + E[w_1'^2] - 2E[w_i' w_1'] \ , \ i = 2, \dots, n \tag{6}$$

Assuming that the noise of the anchors are uncorrelated, the term $E[w_i' w_1']$ will be zero. Defining σ^2 as the variance of the anchors, the final covariance matrix can be summarized as:

$$\begin{bmatrix} \sigma_2^2 + \sigma_1^2 & \sigma_1^2 & \dots & \sigma_1^2 \\ \sigma_1^2 & \sigma_3^2 + \sigma_1^2 & \dots & \sigma_1^2 \\ \dots & \dots & \dots & \dots \\ \sigma_1^2 & \sigma_1^2 & \dots & \sigma_n^2 + \sigma_1^2 \end{bmatrix} \tag{7}$$

As it can be seen, the non-diagonal terms are only correlated to the reference anchor. However, the variance of the diagonal terms are correlated to both anchors. If the noise characteristics in all the anchors are similar, it can be stated that the variance of differential time in star form is two times larger than the variance of noise observed from each anchor.

One major problem of the star form is that, some of the anchors are diagonally linked which means the line of sight of these anchors passes through the area where the mobile nodes are moving. This can cause a non-line of sight (NLOS) case which results in large error in the measurements. It is very hard to determine and compensate this problem in mobile node when the NLOS condition happens between the anchors. The chain form is another anchor pairing style which addresses this problem by linking the nodes that are located on the perimeter of the area. This is demonstrated in Fig. 2.b.

In the chain form, every anchor is paired with its next anchor. Therefore, the next transmission time of each anchor is dependent on the previous anchor. This can be defined for anchors 1 to n according to the following procedure:

$$t_{A_2 tx} = t_{ref} + t_{int} + w_1 \tag{8}$$

$$t_{A_3 tx} = t_{A_2 tx} + t_{int} + w_2 = t_{ref} + 2t_{int} + (w_1 + w_2) \tag{9}$$

$$t_{A_n tx} = t_{A_{n-1} tx} + t_{int} + w_n = t_{ref} + (n-1)t_{int} + (w_1 + w_2 + \dots + w_n) \tag{10}$$

As it can be seen, the noise term of each anchor includes the noise term of previous anchors. For this case, the general form of differential time and its covariance matrix can be defined as:

$$T_{i,(i-1)} = t_{A_{(i-1)} rx} - t_{A_i rx} - t_{int} + w_{(i-1)}' - w_i' \ , \ i = 2, \dots, n \tag{11}$$

$$Q = \begin{bmatrix} \sigma_2^2 + \sigma_1^2 & -\sigma_2^2 & \dots & -\sigma_n^2 \\ -\sigma_2^2 & \sigma_3^2 + \sigma_2^2 & \dots & -\sigma_n^2 \\ \dots & \dots & \dots & \dots \\ -\sigma_n^2 & -\sigma_n^2 & \dots & \sigma_n^2 + \sigma_{n-1}^2 \end{bmatrix} \tag{12}$$

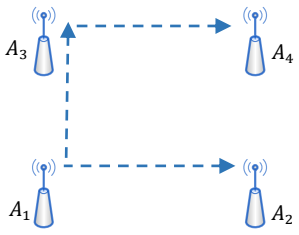

Fig. 3. Hybrid form of anchor pairing with 2 anchors connected according to the star form and one achor according to the chain form

In this case, each non-diagonal term is negatively correlated to the previous anchor and the variance of the diagonal terms are a parameter of the variance of previous anchor. This means, the

https://doi.org/10.24355/dbbs.084-201807191218-1

variance of the last anchor is n times larger than the variance of the first anchor where n is the total number of the anchors in the system. We propose a hybrid pairing style by connecting the anchors according to the star form once they are located on the perimeter of the area, and connecting them according to the chain form when they are diagonally located. This way the NLOS condition is avoided and the variance is pertained at minimum. The hybrid form is depicted in Fig. 3.

According to the hybrid form, the transmission time of the anchors can be defined for four anchors as follows:

$$t_{A_2tx} = t_{ref} + t_{int} + w_1 \tag{13}$$

$$t_{A_3tx} = t_{ref} + 2t_{int} + w_2 \tag{14}$$

$$\begin{aligned} t_{A_4tx} &= t_{A_3tx} + t_{int} + w_3 \\ &= t_{ref} + 3t_{int} + w_2 + w_3 \end{aligned} \tag{15}$$

As it can be seen, in this approach only the variance of the last anchor is increased while the variance of the third and second anchors are constant.

IV. Results and Disscussions

In order to evaluate the amount of the noise variances in practice, a setup including 4 UWB anchors and one mobile node based on each form is developed and the noise range of the received time stamps of the anchors at the mobile node are measured. The transmission interval was 50ms and the area of the filed was 60×40cm². The results for the case of star, chain and hybrid form are provided in Fig. 4, 5 and 6 respectively in cumulative distribution form (CDF). As it is visible in Fig. 4, the distribution of the noise for anchor 2 to 4 are in the same range. This proves the fact that in the star form the variance stays constant as it was stated in the covariance matrix in (7) this is however not the case for chain form as distribution is increasing as the number of anchors increases.

In the proposed hybrid form however, the anchor 4 has larger variance as this node is paired with the anchor 3. Anchor 2 and 3 have similar variances as they are paired according to the star form. In the chain form, the variance of each anchor increases similar to what happened to the anchor 4 in the hybrid form. In the end, it can be concluded that, although the proposed hybrid method has higher variance in one anchor, it has a better performance compared to the chain form and avoids the NLOS problem of the star form.

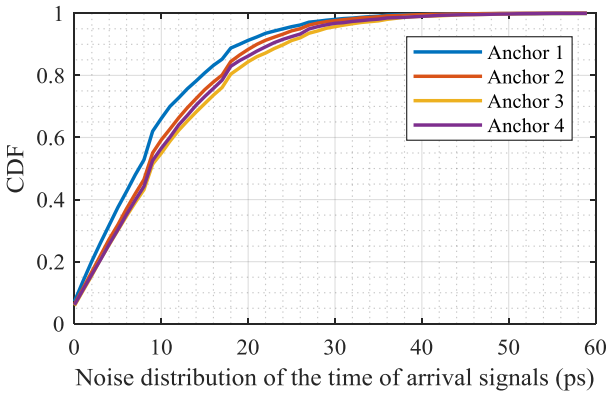

Fig. 4. The noise distribution of the received time stamps for the star form

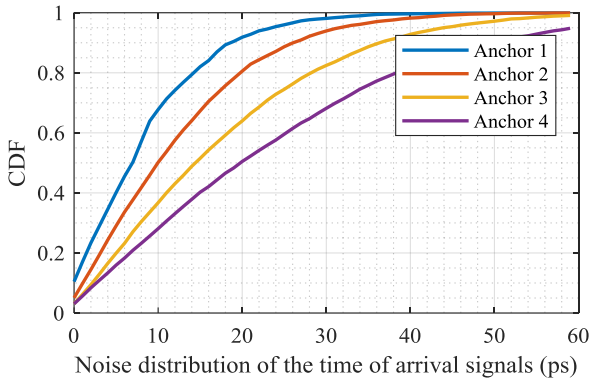

Fig. 5. The noise distribution in the received time stamps for the chain form

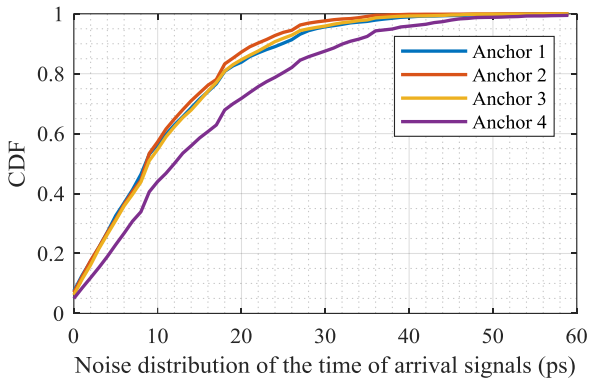

Fig. 6. The noise distribution of the received time stamps for the hybrid form

V. Conclusion

In this paper, common methods of the anchor pair selection in the unilateral TDoA topologies are introduced. The star form is the most common one which uses a common reference for all the nodes. Although this form has constant noise variance for all the anchors, it is disadvantaged from the NLOS problem for some of the anchors. In the chain form, this problem is solved but with the cost of increasing the noise variance linearly with the number of added anchors. The proposed hybrid method has better performance compared to the chain form as only one anchor has higher noise variance. Also the NLOS problem between the anchors is avoided which is an advantage. In case of 3D area with eight anchors, only two of the anchors have higher variance and five of them are paired according to the star form which limits the variance to be constant for those anchors.

References

[1] A. Yassin *et al.,* "Recent Advances in Indoor Localization: A Survey on Theoretical Approaches and Applications," *IEEE Commun. Surv. Tutorials*, vol. 19, no. 2, pp. 1327–1346, 2017.

[2] B. Xu, G. Sun, R. Yu, and Z. Yang, "High-Accuracy TDOA-Based Localization without Time Synchronization," *IEEE Trans. Parallel Distrib. Syst.*, vol. 24, no. 8, pp. 1567–1576, 2013.

[3] J. Kolakowski, J. Cichocki, P. Makal, and R. Michnowski, "An Ultra-Wideband System for Vehicle Positioning," *International Journal of Electronics and Telecommunications*, vol. 56, no. 3, p. 748, 2010.

[4] A. Bensky, *Wireless positioning technologies and applications*. Boston: Artech House, 2016.

[5] R. Zandian and U. Witkowski, "Robot self-localization in ultra-wideband large scale multi-node setups," in *2017 14th Workshop on Positioning, Navigation and Communications (WPNC)*, Bremen, Germany, 2017.

[6] Ł. Żwirełło, *Realization Limits of Impulse-Radio UWB Indoor Localization Systems*. Karlsruhe: KIT Scientific Publishing, 2013.

https://doi.org/10.24355/dbbs.084-201807191218-1

https://doi.org/10.24355/dbbs.084-201807191218-1

Impact of the antenna orientation for distance estimation

Mathias Pelka*, Marco Cimdins* and Horst Hellbrück*†
*Lübeck University of Applied Sciences, Germany
Department of Electrical Engineering and Computer Science
Email: mathias.pelka, marco.cimdins, horst.hellbrueck@fh-luebeck.de
† University of Lübeck, Germany,
Institute of Telematics

***Abstract*—Indoor localization is important for a wide range of use cases including industrial, medical and scientific applications. The location accuracy is affected by the localization algorithm and the quality of the measurements as input for the algorithm. Many indoor localization systems employ ultra-wideband distance measurements, as they offer high accuracy and are cost effective. One of the methods for distance measurement is two-way ranging. This paper investigates the impact of the antenna orientation on the distance measurement based on symmetrical double-sided two-way ranging. We show that up to 0.25 m of the measurement error is attributed to the orientation of the antennas. We provide explanations and suggest solutions to reduce the effect.**

***Index Terms*—signal strength range-bias, antenna orientation, two-way ranging.**

I. Introduction

Precise indoor localization is important for a wide range of applications, including safety-relevant real-time localization. Such systems monitor the location of persons continuously. When a person is located in the proximity of a machinery, the person is warned and eventually, the machinery is stopped. Additional, in emergency situations, save and rescue personnel finds remaining persons more easily with the known location.

Many indoor localization systems employ ultra-wideband distance measurements. Consequentially, accuracy and precision of the distance measurement are crucial for the location estimation. In general, the location error is in the same order of magnitude than the error of the distance measurement, if no additional filtering is applied as shown in the Cramer-Rao lower bound [1] or simulations e.g. [2].

In previous work, we investigated different methods for distance measurements based on plain *two-way ranging*. All distance measurement methods achieve similar results in terms of accuracy and precision. The basic method for two-way ranging is shown in Fig. 1a.

Node A and B exchange messages and calculate the time-of-flight as $t_{\text{tof}} = (t_4 - t_1) - (t_3 - t_2)$. By multiplying the time-of-flight with the propagation speed of the radio wave (namely the speed of light), we calculate the distance between A and B. The variant symmetrical double-sided two-way ranging compensates the clock drift between A and B. However, [3] showed, that with commercial-off-the-shelf hardware, the clock drift is negligible as long as the crystal deviations are below 5 ppm. In that case, all variants of distance measurement methods deliver similar performance in terms of accuracy and precision.

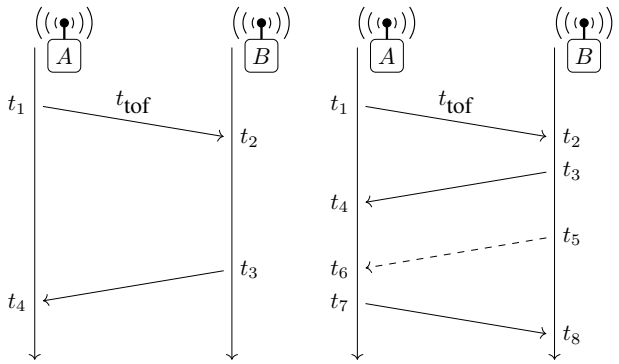

(a) TWR. (b) SDS-TWR.

Fig. 1: Message exchange diagram of two-way ranging (TWR) and symmetrical double-sided two-way ranging (SDS-TWR)

.

The evaluation [3] was carried out under lab conditions, meaning sender and receiver are carefully aligned, to avoid an additional source of error. The alignment of the nodes in Fig. 1a is important as it affects the received signal strength that is correlated to the range-bias [4]. As the antenna gain changes with the orientation, caused by the radiation pattern, this affects the distance measurement.

In this paper, we investigate whether the orientation has an impact on distance measurements and determine the magnitude of this error. A similar investigation was carried out by Ledergerber and D'Andrea in [5]. However, the focus of Ledergerber and D'Andreas work was to model the measurement error rather delivering an explanation.

The rest of the paper is structured as follows: Sec. II presents our measurement setup and Sec. III shows our result. We present explanations for this behavior as well as a solution in Sec. IV and conclude our paper in Sec. V.

II. Measurement Setup

We use the following measurement setup shown in Fig. 2. We place five reference points (white nodes) that are devices

https://doi.org/10.24355/dbbs.084-201807191218-1

with known location and orientation, at the corner of the target area. The orientation is the preferred direction of the radiation pattern of our antenna. We place the tag (black node) at each grid point and measure the distances to each reference point. For each measurement, we rotate the tag clockwise in $90°$ steps. For each point of the grid, we collect 750 measurements. The grid points are 1 m apart, resulting in 20 test points with a total of 60 000 measurements covering 5×4 m.

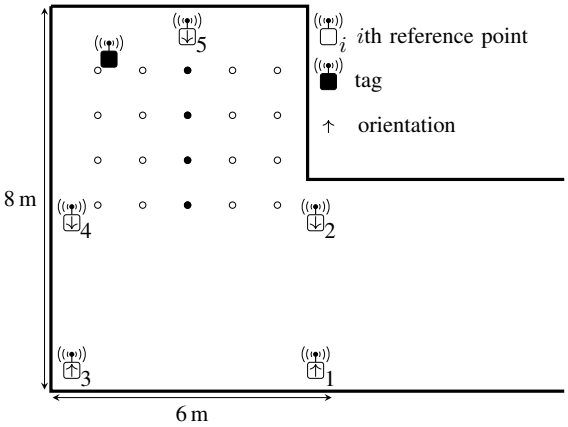

Fig. 2: Measurement setup in our floor.

As the location is known, we calculate the difference μ between the measured distance $\hat{d}$ and the true distance d. In addition to the distance, we record the received signal strength of the first path of the exchanged messages [6].

The hardware for this setup is based on the IEEE 802.15.4a compliant radio unit DWM1000 from Decawave, providing precise timestamping. We perform symmetrical-double-sided two-way ranging, cf. Fig. 1b to measure the distance between the tag and reference points.

III. Evaluation

The empirical cumulative distribution function (CDF) of the measurement error μ (including all orientations and all reference points) is shown in Fig. 3. The mean error is 0.54 m, the median error is 0.47 m, the standard deviation is 0.60 m and the interquartile range (IQR) is 0.30 m. Those measurements values are worse compared to our previously collected measurements in [3], where we derived a mean distance error below 0.10 m. Please mind, that the range bias is not compensated and we only report the raw, unfiltered distance measurements. The mean and median received signal strength is -86 dB, the standard deviation is 3.5 dB and the IQR is 1.8 dB, indicating very stable power measurements.

Next, we choose the 5th reference point and investigate in detail the impact of the orientation to the result. Note, that the remaining reference points show a similar behavior and this discussion is only exemplary. The 5th reference point faces down, according to Fig. 2 and the orientation change is mainly induced due to the rotation of the tag and not when the tags move along the grid. We show the box plots of the measurement error μ in Fig. 4.

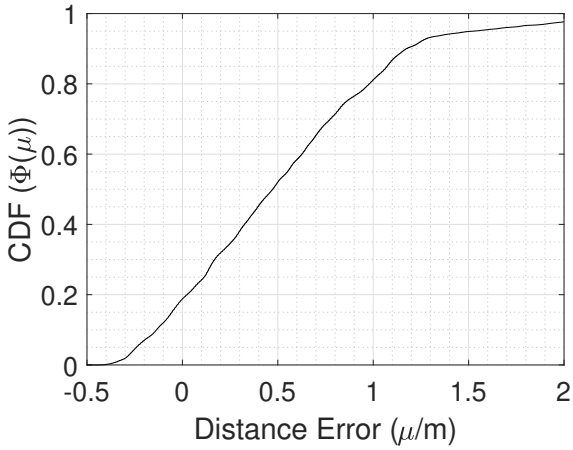

Fig. 3: Empirical cumulative distribution function of the measurement error μ.

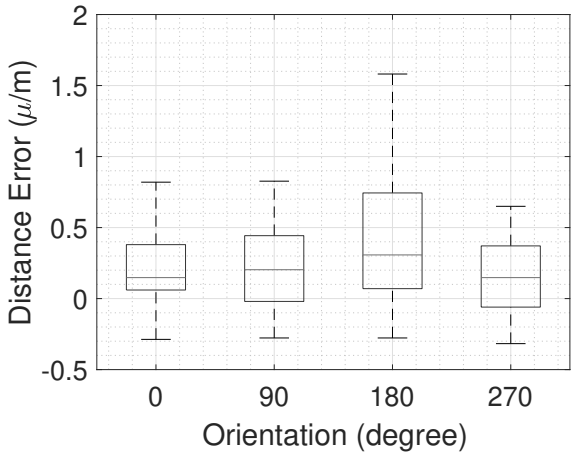

Fig. 4: Boxplot of the measurement error μ for the 5th reference point for all grid points.

The box represents the interquartile range (IQR), which are calculated by the difference of the 75th and the 25th percentile. The central mark indicates the median of the measurement errors. The data enclosed in the whiskers have a length of $1.5\times$ the IQR. In this data set, no outliers are present.

If the orientation does not matter, we would expect that the statistical parameters of each box plot are similar, however, we notice a difference at each investigated orientation. We report the numerical values of the mean, median, standard deviation and IQR in Tab. I. We also report the measured received signal strength for each orientation in Tab. I. Based on symmetry considerations, we expected the $90\,°$ and $270\,°$ to be equal — which proofed wrong. The relative error, which is the difference between the minimum (i.e. 0.16 m) and the maximum (i.e. 0.41 m), is for the mean 0.25 m and for the median 0.16 m. This error is directly induced due to the orientation change. We also note, that the received signal strength does not change with the orientation and is almost constant. In the last evaluation, we evaluate the grid points below the 5th reference point, those are

https://doi.org/10.24355/dbbs.084-201807191218-1

TABLE I: Performance metrics for the 5th reference point for all orientations and grid points.

orientation [°]	0	90	180	270
mean error [m]	0.21	0.23	0.41	0.16
median error [m]	0.15	0.20	0.31	0.15
standard deviation [m]	0.26	0.29	0.39	0.25
IQR [m]	0.32	0.46	0.67	0.43
mean RSSI [dBm]	-85.5	-86.0	-87.0	-85.5
median RSSI [dBm]	-85.5	-85.8	-86.2	-85.4
std RSSI [dB]	3.67	2.69	2.89	3.00
IQR RSSI [dB]	0.96	1.02	2.09	0.91

indicated as filled black dots. In this case, the only parameter we vary is the distance towards the 5th reference point and the orientation of the tag. We report the data in Tab. II. In

TABLE II: Performance metrics for the 5th reference point for all orientations. Only the filled black dots are evaluated.

orientation [°]	0	90	180	270
mean error [m]	0.09	0.15	0.21	0.09
median error [m]	0.13	0.19	0.23	0.13
standard deviation [m]	0.08	0.09	0.12	0.10
IQR 90 [m]	0.10	0.15	0.24	0.17
mean RSSI [dBm]	-85.1	-86.0	-85.7	-85.2
median RSSI [dBm]	-85.2	-86.0	-85.8	-85.2
std RSSI [dB]	3.25	2.45	2.36	2.33
IQR RSSI [dB]	0.66	1.40	0.80	0.72

this case, the orientation is affecting the measurement error, particular at a orientation of $90\,^\circ$ and $180\,^\circ$ The maximum relative error for the mean is 0.12 m and 0.10 m for the median. The received signal strength again is almost constant, similar to Tab. I. Our findings support the measurement of Ledergerber and D'Andrea [5].

IV. Discussion the findings

At a first glance, the signal strength range bias is a reasonable explanation for the behavior. This range bias of the DW1000 is not directly affected by the distance of the reference point and the tag but depends on the received power, which, in return, depends on the distance to each other [4].

If the range bias is the sole explanation for the phenomena, we expect a symmetry in Tab. II, particularly at a orientation of $90\,^\circ$ and $270\,^\circ$. The received signal strength reported in Tab. I did not support this hypothesis. The antenna of the DWM1000 is the ACA-107-T from Abracon. The data sheet from Abracon indicates an almost omnidirectional radiation pattern [7]. Based on the data sheet, the antenna gain due to the orientation is about 10 dB for a frequency of 6.2 GHz. This corresponds to the measured received signal strength variation.

The maximum magnitude of the distance estimation error is between 0.16 m up to 0.41 m, according to Tab. II and Tab. I. The relative error is 0.25 m and caused by the orientation. In contrast, an error of 0.15 m caused by the range bias requires the received signal strength to change by 25 dB, which is not explained by the radiation pattern of the antenna and not supported by the received signal strength measurements [4]. Therefore, we conclude that the range bias is not the explanation of this phenomenon.

An alternative explanation that changing of the orientation affects the rf-propagation path. This results in another accumulated channel impulse response, which is in return evaluated by the DWM1000 to estimate the exact receive time stamp, cf. Fig. 1a and Fig. 1b. This would not directly impact the received signal strength, but only the timestamp.

One possible solution towards this problem includes the incorporation of multiple antennas. Kempke et al. suggested such a solution in [8]. However, one of the main aspects of the DWM1000 is its off-the-shelf availability. Such modifications increase costs, however, for testing of the solution, usage of multiple DWM1000 may prove useful.

V. Conclusion and Future Work

In this paper, we investigated the impact of the orientation towards the distance measurement using symmetrical double-sided two-way ranging. We found that the orientation has an impact towards the distance measurement. In our investigation, the change of the orientation of a tag, caused the distance measurement to change by up to 25 cm. We investigated, whether the signal strength range bias is responsible for this measurement error. Our analysis of the evaluation results shows that this source of error does not explain the measurement error.

We assume that the orientation changes the rf-propagation path and thus influence the distance measurement. To validate this claim we propose to use multiple antennas to investigate this behavior in more detail.

Acknowledgments

This publication is a result of the research work of the Center of Excellence CoSA in the RosiE project (BMWi FKZ ZF4186102ED6). Horst Hellbrück is adjunct professor at the Institute of Telematics of University of Lübeck.

References

[1] Y. Zhao, X. Fan, C.-Z. Xu, and X. Li, "Er-crlb: An extended recursive cramér–rao lower bound fundamental analysis method for indoor localization systems," *IEEE Transactions on Vehicular Technology*, vol. 66, no. 2, pp. 1605–1618, 2017.

[2] M. Pelka, P. Bartmann, S. Leugner, and H. Hellbrück, "Minimizing indoor localization errors for non-line-of-sight propagation," in *8th International Conference on Localization and GNSS*. IEEE, 2018.

[3] M. Pelka, D. Amann, M. Cimdins, and H. Hellbrück, "Evaluation of time-based ranging methods: Does the choice matter?" in *14th Workshop on Positioning, Navigation and Communication*. IEEE, 2017.

[4] Decawave, "Sources of error in two way ranging," 2018. [Online]. Available: https://www.decawave.com/content/sources-error-two-way-ranging

[5] A. Ledergerber and R. D'Andrea, "Ultra-wideband range measurement model with gaussian processes," in *Control Technology and Applications (CCTA), 2017 IEEE Conference on*. IEEE, 2017.

[6] Decawave, "Dw1000 user manual, section 4.7.1," 2018. [Online]. Available: https://www.decawave.com/content/dw1000-user-manual

[7] Abracon, "Antenna aca-1007-t," 2018. [Online]. Available: https://abracon.com/uploads/resources/ACA-107-T-ApplicationNote.pdf

[8] B. Kempke, P. Pannuto, and P. Dutta, "Polypoint: Guiding indoor quadrotors with ultra-wideband localization," in *Proceedings of the 2nd International Workshop on Hot Topics in Wireless*. ACM, 2015.

https://doi.org/10.24355/dbbs.084-201807191218-1

https://doi.org/10.24355/dbbs.084-201807191218-1

Evaluation of H-infinity Filter in Time Differential Localization Systems

Reza Zandian, Ulf Witkowski
Department of Circuits Design and Electronics
South Westphalia University of Applied Science
Soest, Germany
Email: {zandian.reza, witkowski}@fh-swf.de

***Abstract*— This paper evaluates the performances of H_∞ filter in differential time of arrival (TDoA) localization applications and compares the results with other filters such as extended Kalman filter (EKF) and unscented Kalman filter (UKF) in practical trials. The filters are compared in ideal as well as non-ideal conditions such as different positive and negative values of initial points, presence of erroneous data and excessive noise. The results show that, the H_∞ filter is sub-optimal in ideal conditions as the other filters outperform this filter, but once the initial points are badly selected or data are erroneous, the filter is more robust and accurate than the other variants. Considering the challenging conditions of the indoor environment, use of this filter in localization systems seems to be a good choice.**

Keywords— Localization, TDoA, EKF, UKF, H-infinity filter

I. INTRODUCTION

Kalman-based family of filters are very flexible, accurate and effective type of estimators which have been applied successfully in many projects especially in the localization applications in the last few decades [1]. Among these filters, the extended Kalman filter (EKF) is commonly used for nonlinear cases. This filter benefits from Jacobian linearization process that extracts the first moment of the Taylor series to define a linear matrix at the operation point of the non-linear model. As in this process, the higher orders of the Taylor series are ignored, this filter is known to be sub-optimal in highly non-linear conditions. One solution to this problem is second order EKF (SOEKF) which considers the second term in Taylor series yielding in higher accuracy of the filter with the cost of higher computation time and complexity [2]. Other heuristic methods such as unscented Kalman filter (UKF) can also be applied which does not use Jacobian process, rather extracts the model characteristics statistically. The UKF is more accurate than the EKF as in this method also the second moment of the non-linear function is held.

One major requirement of the mentioned filters is a noise with zero mean and Gaussian distribution. Under conditions where the Gaussian requirement is not met, or model of the system is inaccurately defined, or the measured data are erroneous, the filter may diverge. Many efforts are invested to improve the stability of the filters in such conditions. One solution is a robust Kalman filter known as H_∞ filter which is designed specifically for robustness. Unlike the Kalman filter which is designed to estimate the mean of the power, the H_∞ filter limits the maximum power of the noise to a worst case condition. In addition to that, the H_∞ filter does not make any assumption about the noise characteristics as these parameters are defined deterministically. This is a very advantages feature as in many applications these parameters are not known in advance and the noise characteristics may also change during the operation of the system [3].

A few researchers have studied the performances of the H_∞ filter and compared it with other filtering approaches. Examples of comparison of H_∞ filter with Kalman filter are provided in [2, 4, 5]. Cao et al. [6] have applied H_∞ filter for blind navigation application. Other papers who address application of H_∞ filter in localization area are [1, 7, 8]. Also modified version of H_∞ filter such as unscented H_∞ filter or adaptive H_∞ filter are proposed in the works [9, 10].

Although the performance of this filter has been addressed before, most of these evaluations are done only theoretically or by simulation. This paper addresses the application of H_∞ filter in time differential localization systems and compares the general performances of this filter in terms of accuracy, runtime speed, convergence speed and resistivity against non-ideal conditions with EKF and UKF in practical experiments.

II. STRUCTURE OF THE H_∞ FILTER

The application of H_∞ filter for non-linear systems is similar to EKF in that Jacobian process is applied for linearization. The result is extended H_∞ filter which is exploited in our project for localization of robots in a differential time of arrival (TDoA) localization system. The model of a localization system in the form of state space can be defined as:

$$x_{k+1}^- = Ax_k + w_k \tag{1}$$

$$y_{k+1} = h(x_{k+1}^-) + v_k \tag{2}$$

where x_{k+1}^- is the *a priori* matrix of the state variables after prediction including the location and speed of the mobile node in each axis, A is the fundamental matrix of the model which defines the dynamics of the node, y is the differential distance measurements of the node, and w and v are the process noise and measurement noise respectively. The non-linear observation function h in TDoA topology is defined according to the following equation:

$$d_{m,n} = \sqrt{(x - x_m)^2 + (y - y_m)^2} - \sqrt{(x - x_n)^2 + (y - y_n)^2} \tag{3}$$

https://doi.org/10.24355/dbbs.084-201807191218-1

where (x, y) are coordinates of the mobile node, (x_m, y_m) and (x_n, y_n) are coordinates of the anchors m and n respectively and $d_{m,n}$ is the differential range between the mobile node and the anchors m and n. The first step of the filter, is to linearize the nonlinear function h around the states operating point x_k using Jacobian which is defined as:

$$H_k = \left.\frac{\partial h(x)}{dx}\right|_{x_k} \tag{4}$$

The H_∞ filter defines a bound to the maximum energy of the noise by defining following equation:

$$D_k = (I - \gamma S_k P_k + H_k^T R_k^{-1} H_k P_k)^{-1} \tag{5}$$

where I is the identity matrix, P_k is the error of the estimate, the matrices S_k and R_k are defined by user deterministically and γ is the defined bound which limits the noise and model error worst cases. This parameter is a value close to zero which should be selected carefully according to the application to avoid filter divergence. In the next step, the filter gain is defined as:

$$K_k = A_k P_k D_k H_k^T R_k^{-1} \tag{6}$$

The final steps of the filter are prediction and update which are described below together with the error estimate equation as:

$$\hat{x}_{k+1} = A_k \hat{x}_k + K_k\big(y_k - h(\hat{x}_k)\big) \tag{7}$$

$$P_{k+1} = A_k P_k D_k A_k^T + Q_k \tag{8}$$

where Q is also a matrix defined and acquired empirically by user to avoid covariance matrix P_{k+1} converging to zero.

III. Perfromance Evaluation and Experiments

In the first experiment, the amount of localization noise for each filtering algorithm in ideal conditions is evaluated. For this purpose, a stationary node is used which was located in the middle of a test field with dimensions of $60 \times 40\text{cm}^2$ and surrounded by 4 anchors located at each corner of the field. The standard deviation of the measurements are provided in the form of probability distribution function (PDF) in Fig. 1. The amount of observed noise for these filtering techniques are almost identical with a mean value of 2.66 for EKF, 2.68 for UKF and 2.64 for H_∞ filter. The distribution of the noise in all cases is Rician with mean 2.39 and variance of 1.32.

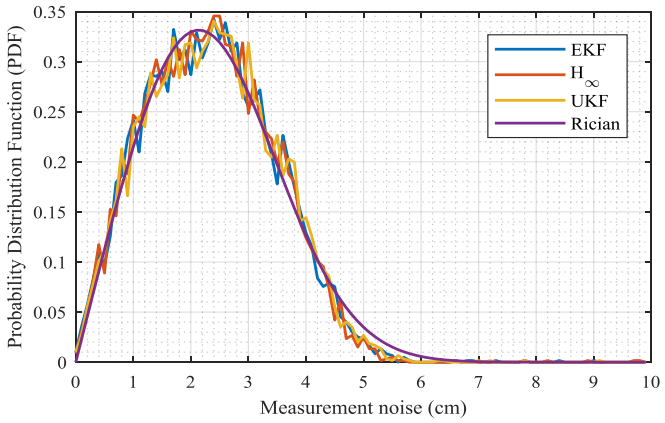

Fig. 1. The standard deviation of the noise in location measurements of different filtering techniques with Rician distribution

In the next experiment, the effect of initial point on the convergence of filters are evaluated. For the case of the fixed node which is used in the previous setup, different initial points are considered. These are (1,1), (80,50), (-10,80), (-1,-5). The real position of the node is (34,20). The selection of the initial points are based on criteria such as distance and different sign of the location to evaluate the behavior of filter in these complex conditions. The results of filter convergence for the mentioned methods and only axis x are provided in Fig. 2. For the case of initial point (1,1) (Fig.2.a) all the filters converge quickly with faster convergence of EKF. This is an ideal condition for filters as the initial values are positive, in the vicinity of the target and smaller than the final value. For the next initial point (80,50), the filters need to decrease the value of axis x. In this case, the UKF has a better performance by converging immediately to close vicinity of the target point. The EKF needs more time and tends to be unstable in this case. These bounces are however minimum for H_∞ filter. For the next point (-10,80), one negative number is provided which results in divergence of UKF. In the last step, both values are negative which again results in divergence of UKF as well as instability of EKF. The superior behavior of H_∞ filter in these cases are clearly visible. As a conclusion, it can be deducted that the H_∞ filter has robust behavior when the initial points are badly selected, however when the points are ideally selected, the performances of other filters could be better.

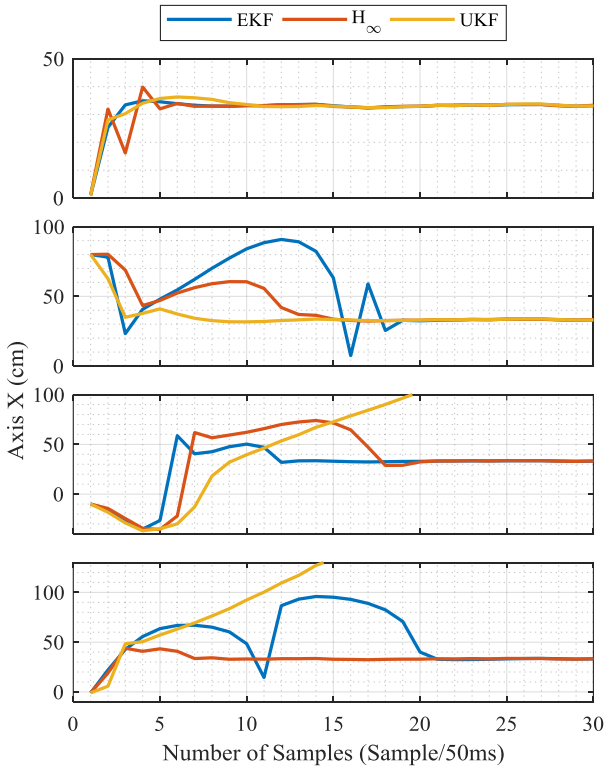

Fig. 2. Convergence speed and behaviour of different filters for different initial points from top to bottom (1,1), (80,50), (-10,80), (-1,-5)

In the next experiment, the effect of erroneous data on the filter's performance is evaluated. For this sake, a barrier is used to block the line of sight between the stationary node used in the setup and the anchor nodes to simulate non-line of sight (NLOS) conditions. These conditions normally create a large bias error

https://doi.org/10.24355/dbbs.084-201807191218-1

in the distance measurements which in some cases result in filter divergence. In our experiment, we have created a severe NLOS condition which resulted in large bias error. The results of node localization for the filters are provided in Fig. 3. As it can be seen, this error resulted in divergence of the UKF. Also the EKF is largely deviated from the real point of the node with error of around 20m, but still could manage to return to the real point when the NLOS condition is removed. Unlike the other filters, H_∞ filter resists against the non-ideal and erroneous data measurements and only experiences an error of 2m.

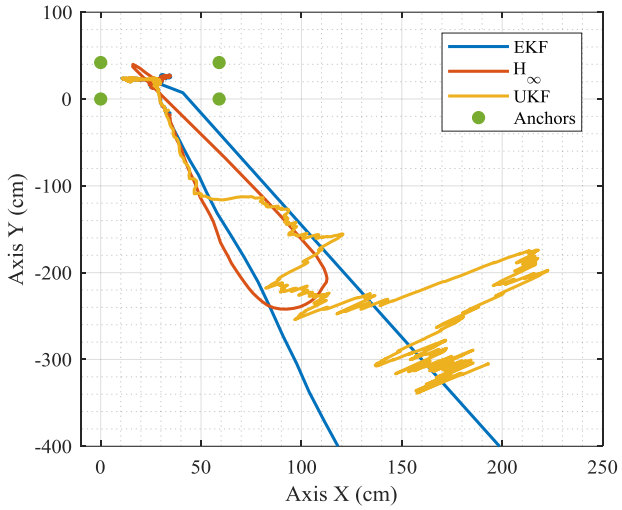

Fig. 3. Localization results of a stationary node with NLOS condition

The localization error of this experiment for different filters are presented in Fig. 4. According to the results, it can be seen that the H_∞ filter mitigates the error of the localization about one sixth of the EKF and avoids divergence of the filter.

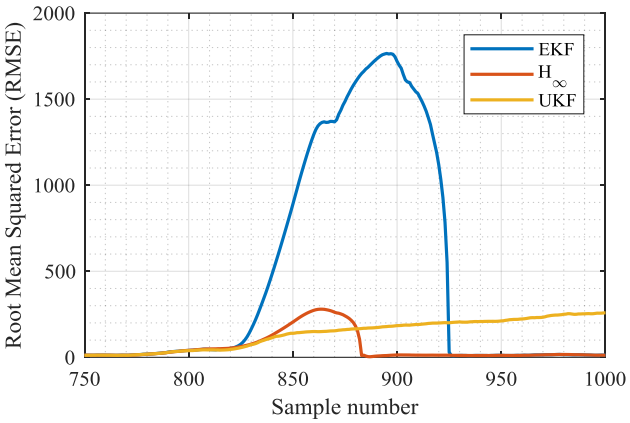

Fig. 4. Localization error of different filter for a node in NLOS condition

The performance of the H_∞ filter in terms of runtime as well as implementation complexity is evaluated. The results are provided in Table I. According to these results, the fastest runtime belongs to EKF. The H_∞ filter is slightly slower than EKF but still is twice faster than the UKF. Due to the structure of the UKF which needs to integrates sigma points and evaluates the noise characteristics at each iteration, the runtime of this algorithm is long and the filter has the highest implementation complexity among the other filters.

TABLE I. COMPARISON OF THE FILTERS' CHARACTERISTICS

Parameter	***EKF***	***UKF***	***H_∞***
Minimum runtime	20.52 μs	71.84 μs	39.91 μs
Implementation complexity	Low	High	Medium

IV. CONCLUSION

In this paper, the robust H_∞ filter is introduced and its performances against other common filtering methods namely EKF and UKF which are used for localization systems are compared. The filters are evaluated in a series of practical experiments with the focus on analyzing the behavior of the filter in non-ideal and presence of erroneous measurements. The results of experiments indicated that, the H_∞ filter is robust against badly selected initial points but sub-optimal when the conditions are ideal. Also in case of presence of erroneous data such as NLOS conditions, the filter shows resistance against divergence and introduces only a small portion of deviation (1/6) compared to EKF. As a conclusion, it can be stated that, the H_∞ filter proves to be a good choice for challenging conditions of localization systems especially in indoor area where the NLOS condition is highly expected. Although the filter is sub-optimum in ideal conditions, the robustness of the filter is promising with slightly longer runtime but smaller implementation overhead compared to UKF algorithm.

REFERENCES

[1] C. Jiang, S.-B. Zhang, and Q.-Z. Zhang, "A New Adaptive H-Infinity Filtering Algorithm for the GPS/INS Integrated Navigation," *Sensors (Basel, Switzerland)*, vol. 16, no. 12, 2016.

[2] Héctor Poveda, Guillaume Ferré, Eric J. Grivel, Nicolai Christov, "Kalman Vs H∞ Filter in Terms of Convergence and Accuracy: Application to CFO Estimation," *20th European Signal Processing Conference (EUSIPCO 2012)*, vol. 20, pp. 121–125, 2012.

[3] D. Simon, "From Here to Infinity," *Embedded Systems Programming*, vol. 14, no. 11, 2000.

[4] Rawicz and Lawrence Paul, "H [infinity symbol]/H2/Kalman filtering of linear dynamical systems via variational techniques with applications to target tracking," PhD, Drexel University, Philadelphia, Pennsylvania, USA, 2000.

[5] P. Batista, C. Silvestre, and P. Oliveira, "Kalman and H∞ Optimal Filtering for a Class of Kinematic Systems," *IFAC Proceedings Volumes*, vol. 41, no. 2, pp. 12528–12533, 2008.

[6] F. C. Cao, G. L. Cheng, and L. R. Wang, "A Tracking Algorithm for Blind Navigation Based on Robust H Infinity Filter," *AMM*, vol. 448-453, pp. 3580–3585, 2013.

[7] F. Yang, Z. Wang, S. Lauria, and X. Liu, "Mobile robot localization using robust extended H∞ filtering," *Proceedings of the Institution of Mechanical Engineers, Part I: Journal of Systems and Control Engineering*, vol. 223, no. 8, pp. 1067–1080, 2009.

[8] Y. Zhuang, Z. Wang, H. Yu, W. Wang, and S. Lauria, "A robust extended filtering approach to multi-robot cooperative localization in dynamic indoor environments," *Control Engineering Practice*, vol. 21, no. 7, pp. 953–961, 2013.

[9] K. Xiong, H. Zhang, and L. Liu, "Adaptive Robust Extended Kalman Filter," in *Kalman Filter Recent Advances and Applications*, V. M. and A. Pigazo, Eds.: InTech, 2009.

[10] W. Li and Y. Jia, "H-infinity filtering for a class of nonlinear discrete-time systems based on unscented transform," *Signal Processing*, vol. 90, no. 12, pp. 3301–3307, 2010.

https://doi.org/10.24355/dbbs.084-201807191218-1

https://doi.org/10.24355/dbbs.084-201807191218-1

Theoretical Considerations Regarding the Application of Received Signal Strength within Heterogeneous Indoor Positioning Systems

Marco Gunia*, Niko Joram* and Frank Ellinger*
*Chair of Circuit Design and Network Theory (CCN)
Technische Universität Dresden, 01062 Dresden
Email: marco.gunia@tu-dresden.de

***Abstract*—Nowadays, there are a variety of different indoor positioning systems, where some of them use communication hardware taking advantage of the Received Signal Strength (RSS) such as Wireless Local Area Networks (WLAN) or Bluetooth. These variants are employed if low cost is of primary importance. However, the accuracy provided is in the meter range. The alternative are positioning-tailored approaches like Frequency Modulated Continuous Wave (FMCW) radar, Ultra-WideBand (UWB) radar or phase-based positioning, which offer superior accuracy in the low decimetre range. If there is such a system in use, the question arises whether there is any improvement, if utilizing additional RSS measurements, which are performed by most systems anyway. With the help of the Cramér-Rao Lower Bound (CRLB), this paper demonstrates that these additional readings can improve accuracy significantly, thus widen the application field for RSS from a low-budget only technique to enabling enhanced accurate positioning. To demonstrate this statement we compare the CRLB for Time of Arrival (ToA) with hybrid ToA/RSS. Our evaluations show that in practice the CRLB is approximately divided by two, if incorporating the RSS for each base station.**

***Keywords*—Localization, Positioning, Cramér Rao Lower Bound, CRLB, Time of Arrival, ToA, Received Signal Strength, RSS, Hybrid ToA/RSS**

I. Introduction

TODAY there are two main fields of research for indoor positioning systems. On the one hand, there are techniques taking advantage of already available infrastructure to estimate the unknown position of a user. These approaches frequently utilize the RSS of systems originally set up for communication, e.g. WLAN [1], Bluetooth [2] or ZigBee [3] with mean positioning error above 1 m. Although we limit our considerations within this paper to RSS, there are other related variants. As an example, a system employing the Internet Protocol (IP) addresses for geo-localization is presented in [4]. In short, in this category the underlying hardware is not altered but reused.

The alternative are approaches particularly built for positioning. Examples include FMCW radar [5], UWB radar [6] or ZigBee phase-based positioning [7]. At the expense of sophisticated infrastructure, they offer superior results with positioning errors in the low decimetre range.

Within this paper we show that even though RSS-based variants are inferior, their incorporation can significantly increase the accuracy for position-tailored techniques. These RSS measurements are usually generated anyway, e.g. to check if a minimal receiving power is available to perform ranging measurements.

The rest of this paper is organized as follows. Section II presents the mathematical basics. The CRLB for selected variants are derived in section III and IV. In the next section V, the CRLBs are compared by means of evaluations and the initial claim is verified. The last section VI concludes the paper.

II. Statistical Foundations

In the further course of this paper we use the following designators. A vector is denoted by a bold lower italic letter (e.g. $\boldsymbol{b}$), whereas matrices employ bold italic capital letters (e.g. $\boldsymbol{B}$). The symbol $\tilde{\cdot}$ indicates random variables (e.g. $\tilde{X}$) and the prefix ${}^{E}\cdot$ is used to characterize an estimator, which is generally also a random variable (e.g. ${}^{E}\tilde{X}$).

The CRLB specifies a lower bound for the covariance matrix of any unbiased estimator ${}^{E}\tilde{\boldsymbol{\theta}}$ for the unknown parameter $\boldsymbol{\theta} = (\theta_1, \ldots, \theta_{\mathrm{N}})^T$, i.e. [8]

$$\mathbb{COV}\left[{}^{E}\tilde{\boldsymbol{\theta}}\right] - \boldsymbol{F}^{-1}(\boldsymbol{\theta}) \geq 0 \tag{1}$$

Here, $\mathbb{COV}\left[{}^{E}\tilde{\boldsymbol{\theta}}\right]$ denotes this covariance matrix. Moreover, the inverse of the Fisher information matrix $\boldsymbol{F}(\boldsymbol{\theta})$ is required, where the element in the i-th row and j-th column reads

$$[\boldsymbol{F}(\boldsymbol{\theta})]_{(i,j)} = -\mathbb{E}\left[\frac{\partial^2 \ln\left(f(\tilde{\boldsymbol{M}}|\boldsymbol{\theta})\right)}{\partial\theta_i \partial\theta_j}\right] \tag{2}$$

Above, we have taken into account that the unknown $\boldsymbol{\theta}$ might only be determined by means of some intermediate measurement vector $\tilde{\boldsymbol{M}} = \left(\tilde{M}_1, \ldots, \tilde{M}_{\mathrm{N}}\right)^T$.

III. Cramér Rao Lower Bounds

Below, we derive the CRLB for ToA, RSS and ToA/RSS, since the CRLB specifies the theoretical optimum for any unbiased estimator utilizing these approaches. This enables to evaluate the performance for an arbitrary positioning system utilizing one of these techniques.

https://doi.org/10.24355/dbbs.084-201807191218-1

A. Time of Arrival

The CRLB is derived for the localization of a Mobile Station (MS) which measures the transmission time $t_{i\leftrightarrow\bullet}$ to every Base Station (BS) i, where $i = 1, \ldots, \mathrm{N}$. We assume that these readings are Gaussian with constant measurement variance σ_{T}^2 for all BS, i.e.

$$\tilde{t}_{i\leftrightarrow\bullet} \sim \mathcal{N}\left(\frac{d_{i\leftrightarrow\bullet}}{\mathrm{c}}, \sigma_{\mathrm{T}}^2\right) \tag{3}$$

The associated true distance to the i-th BS is denoted as $d_{i\leftrightarrow\bullet} = \sqrt{(x_i - x_\bullet)^2 + (y_i - y_\bullet)^2}$, where $(x_\bullet, y_\bullet)$ is the sought unknown true position of the MS. In eq. (3), c is the speed of light. Hence, the conditional probability density function (p.d.f.) can be written as

$$f(\tilde{t}_{i\leftrightarrow\bullet}|x_\bullet, y_\bullet) = \frac{1}{\sqrt{2\pi}\sigma_{\mathrm{T}}}\exp\left(-\frac{1}{2\sigma_{\mathrm{T}}^2}\left[\tilde{t}_{i\leftrightarrow\bullet} - \frac{d_{i\leftrightarrow\bullet}}{\mathrm{c}}\right]^2\right) \tag{4}$$

It is reasonable to assume that all N single measurements $\tilde{t}_{i\leftrightarrow\bullet}$ are stochastically independent. Thus, the joint p.d.f. reads

$$f(\tilde{\boldsymbol{t}}|x_\bullet, y_\bullet) = \prod_{i=1}^{\mathrm{N}} f(\tilde{t}_{i\leftrightarrow\bullet}|x_\bullet, y_\bullet) \tag{5}$$

where $\tilde{\boldsymbol{t}} = (\tilde{t}_{1\leftrightarrow\bullet}, \ldots, \tilde{t}_{\mathrm{N}\leftrightarrow\bullet})^T$ is a vector combining these time measurements. For determining the CRLB, we calculate the logarithmic joint p.d.f. $l(\tilde{\boldsymbol{t}}|x\bullet, y\bullet)$, which is defined as

$$\begin{aligned} &l(\tilde{\boldsymbol{t}}|x_\bullet, y_\bullet) := \ln\left(f(\tilde{\boldsymbol{t}}|x_\bullet, y_\bullet)\right) \\ &= \ln\left(\prod_{i=1}^{\mathrm{N}}\left\{\frac{1}{\sqrt{2\pi}\sigma_{\mathrm{T}}}\exp\left(-\frac{1}{2\sigma_{\mathrm{T}}^2}\left[\tilde{t}_{i\leftrightarrow\bullet} - \frac{d_{i\leftrightarrow\bullet}}{\mathrm{c}}\right]^2\right)\right\}\right) \\ &= \mathrm{N}\cdot\ln\left(\frac{1}{\sqrt{2\pi}\sigma_{\mathrm{T}}}\right) - \frac{1}{2\sigma_{\mathrm{T}}^2}\sum_{i=1}^{\mathrm{N}}\left(\tilde{t}_{i\leftrightarrow\bullet} - \frac{d_{i\leftrightarrow\bullet}}{\mathrm{c}}\right)^2 \end{aligned} \tag{6}$$

Above, eq. (4) and (5) are employed along with the well-known logarithmic identities. According to eq. (1), the inverse of

$$\boldsymbol{F}(\boldsymbol{\theta}) = \boldsymbol{F}(x_\bullet, y_\bullet) = \begin{bmatrix} F_{x_\bullet x_\bullet} & F_{x_\bullet y_\bullet} \\ F_{y_\bullet x_\bullet} & F_{y_\bullet y_\bullet} \end{bmatrix} \tag{7}$$

is required, where the matrix elements are characterized as

$$\begin{aligned} F_{x_\bullet x_\bullet} &= -\mathbb{E}\left[\frac{\partial^2 l(\tilde{\boldsymbol{t}}|x_\bullet, y_\bullet)}{\partial x_\bullet^2}\right] & F_{x_\bullet y_\bullet} &= -\mathbb{E}\left[\frac{\partial^2 l(\tilde{\boldsymbol{t}}|x_\bullet, y_\bullet)}{\partial x_\bullet \partial y_\bullet}\right] \\ F_{y_\bullet y_\bullet} &= -\mathbb{E}\left[\frac{\partial^2 l(\tilde{\boldsymbol{t}}|x_\bullet, y_\bullet)}{\partial y_\bullet^2}\right] & F_{y_\bullet x_\bullet} &= F_{x_\bullet y_\bullet} \end{aligned} \tag{8}$$

Performing the second order derivation for $x_\bullet$ yields

$$\begin{aligned} &\frac{\partial^2 l(\tilde{\boldsymbol{t}}|x_\bullet, y_\bullet)}{\partial x_\bullet^2} \\ &= -\frac{1}{\mathrm{c}\cdot\sigma_{\mathrm{T}}^2}\sum_{i=1}^{\mathrm{N}}\left[\frac{(x_i - x_\bullet)^2}{\mathrm{c}\cdot d_{i\leftrightarrow\bullet}^2} + \frac{(x_i - x_\bullet)^2\left(\tilde{t}_{i\leftrightarrow\bullet} - \frac{d_{i\leftrightarrow\bullet}}{\mathrm{c}}\right)}{d_{i\leftrightarrow\bullet}^3} - \frac{\left(\tilde{t}_{i\leftrightarrow\bullet} - \frac{d_{i\leftrightarrow\bullet}}{\mathrm{c}}\right)}{d_{i\leftrightarrow\bullet}}\right] \end{aligned} \tag{9}$$

Equally,

$$\begin{aligned} &\frac{\partial^2 l(\tilde{\boldsymbol{t}}|x_\bullet, y_\bullet)}{\partial y^2} \\ &= -\frac{1}{\mathrm{c}\cdot\sigma_{\mathrm{T}}^2}\sum_{i=1}^{\mathrm{N}}\left[\frac{(y_i - y_\bullet)^2}{\mathrm{c}\cdot d_{i\leftrightarrow\bullet}^2} + \frac{(y_i - y_\bullet)^2\left(\tilde{t}_{i\leftrightarrow\bullet} - \frac{d_{i\leftrightarrow\bullet}}{\mathrm{c}}\right)}{d_{i\leftrightarrow\bullet}^3} - \frac{\left(\tilde{t}_{i\leftrightarrow\bullet} - \frac{d_{i\leftrightarrow\bullet}}{\mathrm{c}}\right)}{d_{i\leftrightarrow\bullet}}\right] \end{aligned} \tag{10}$$

And for the mixed second order derivations for $x_\bullet$ and $y_\bullet$:

$$\begin{aligned} &\frac{\partial^2 l(\tilde{\boldsymbol{t}}|x_\bullet, y_\bullet)}{\partial y_\bullet \partial x_\bullet} \\ &= -\frac{1}{\mathrm{c}\cdot\sigma_{\mathrm{T}}^2}\sum_{i=1}^{\mathrm{N}}\left[-\frac{(x_i - x_\bullet)\cdot(y_i - y_\bullet)}{\mathrm{c}\cdot d_{i\leftrightarrow\bullet}^2} - \frac{(x_i - x_\bullet)\cdot(y_i - y_\bullet)\left(\tilde{t}_{i\leftrightarrow\bullet} - \frac{d_{i\leftrightarrow\bullet}}{\mathrm{c}}\right)}{d_{i\leftrightarrow\bullet}^3}\right] \end{aligned} \tag{11}$$

Due to the underlying Gaussian distribution, we have

$$\mathbb{E}\left[\tilde{t}_{i\leftrightarrow\bullet}\right] = \frac{d_{i\leftrightarrow\bullet}}{\mathrm{c}} \tag{12}$$

and thus the elements of the Fisher information matrix $\boldsymbol{F}(x_\bullet, y_\bullet)$ read

$$F_{x_\bullet x_\bullet} = -\mathbb{E}\left[\frac{\partial^2 l(\tilde{\boldsymbol{t}}|x_\bullet, y_\bullet)}{\partial x_\bullet^2}\right] = \mathrm{K_S}\sum_{i=1}^{\mathrm{N}}\left[\frac{(x_i - x_\bullet)^2}{d_{i\leftrightarrow\bullet}^2}\right] \tag{13}$$

$$F_{x_\bullet y_\bullet} = -\mathbb{E}\left[\frac{\partial^2 l(\tilde{\boldsymbol{t}}|x_\bullet, y_\bullet)}{\partial y_\bullet \partial x_\bullet}\right] = -\mathrm{K_S}\sum_{i=1}^{\mathrm{N}}\left[\frac{(x_i - x_\bullet)(y_i - y_\bullet)}{d_{i\leftrightarrow\bullet}^2}\right] \tag{14}$$

$$F_{y_\bullet y_\bullet} = -\mathbb{E}\left[\frac{\partial^2 l(\tilde{\boldsymbol{t}}|x_\bullet, y_\bullet)}{\partial y_\bullet^2}\right] = \mathrm{K_S}\sum_{i=1}^{\mathrm{N}}\left[\frac{(y_i - y_\bullet)^2}{d_{i\leftrightarrow\bullet}^2}\right] \tag{15}$$

To simplify, we have set above

$$\mathrm{K_S} := \frac{1}{\mathrm{c}^2\cdot\sigma_{\mathrm{T}}^2} \tag{16}$$

For the CRLB we need to determine the inverse of this matrix, which can be written as [9]

$$\boldsymbol{F}^{-1}(x_\bullet, y_\bullet) = \frac{1}{F_{x_\bullet x_\bullet}\cdot F_{y_\bullet y_\bullet} - F_{x_\bullet y_\bullet}^2}\begin{bmatrix} F_{y_\bullet y_\bullet} & -F_{x_\bullet y_\bullet} \\ -F_{y_\bullet x_\bullet} & F_{x_\bullet x_\bullet} \end{bmatrix} \tag{17}$$

The CRLB for an unbiased estimator $({}^E\tilde{x}_\bullet, {}^E\tilde{y}_\bullet)$ is given according to eq. (1) as

$$\mathbb{COV}\left[{}^E\tilde{x}_\bullet, {}^E\tilde{y}_\bullet\right] - \boldsymbol{F}^{-1}(x_\bullet, y_\bullet) \geq 0 \tag{18}$$

where the covariance matrix $\mathbb{COV}\left[{}^E\tilde{x}_\bullet, {}^E\tilde{y}_\bullet\right]$ reads

$$\begin{aligned} &\mathbb{COV}\left[{}^E\tilde{x}_\bullet, {}^E\tilde{y}_\bullet\right] \\ &= \begin{bmatrix} \mathbb{E}\left[({}^E\tilde{x}_\bullet - x_\bullet)^2\right] & \mathbb{E}\left[({}^E\tilde{x}_\bullet - x_\bullet)({}^E\tilde{y}_\bullet - y_\bullet)\right] \\ \mathbb{E}\left[({}^E\tilde{y}_\bullet - y_\bullet)({}^E\tilde{x}_\bullet - x_\bullet)\right] & \mathbb{E}\left[({}^E\tilde{y}_\bullet - y_\bullet)^2\right] \end{bmatrix} \end{aligned} \tag{19}$$

We seek a lower bound for the expectation of the positioning error $\mathbb{E}\left[({}^E\tilde{x}_\bullet - x_\bullet)^2 + ({}^E\tilde{y}_\bullet - y_\bullet)^2\right]$. Due to the linearity of the expectation operator, we can reduce this problem to finding

https://doi.org/10.24355/dbbs.084-201807191218-1

the errors $\mathbb{E}\left[({}^{E}\tilde{x}_\bullet - x_\bullet)^2\right]$ and $\mathbb{E}\left[({}^{E}\tilde{y}_\bullet - y_\bullet)^2\right]$. For these, we insert inequality (18), respectively, to yield the CRLB [10]

$$\begin{aligned}
&\mathbb{E}\left[({}^{E}\tilde{x}_\bullet - x_\bullet)^2 + ({}^{E}\tilde{y}_\bullet - y_\bullet)^2\right] \\
&= \mathbb{E}\left[({}^{E}\tilde{x}_\bullet - x_\bullet)^2\right] + \mathbb{E}\left[({}^{E}\tilde{y}_\bullet - y_\bullet)^2\right] \\
&\geq \frac{F_{x_\bullet x_\bullet}}{F_{x_\bullet x_\bullet}\cdot F_{y_\bullet y_\bullet} - F_{x_\bullet y_\bullet}^2} + \frac{F_{y_\bullet y_\bullet}}{F_{x_\bullet x_\bullet}\cdot F_{y_\bullet y_\bullet} - F_{x_\bullet y_\bullet}^2} \\
&= \frac{\sum_{i=1}^{\mathrm{N}}\left[\frac{(x_i - x_\bullet)^2}{d_{i\leftrightarrow\bullet}^2}\right] + \sum_{i=1}^{\mathrm{N}}\left[\frac{(y_i - y_\bullet)^2}{d_{i\leftrightarrow\bullet}^2}\right]}{\mathrm{K_S}\left\{\begin{array}{l}\left[\sum_{i=1}^{\mathrm{N}}\left[\frac{(x_i - x_\bullet)^2}{d_{i\leftrightarrow\bullet}^2}\right]\cdot\sum_{i=1}^{\mathrm{N}}\left[\frac{(y_i - y_\bullet)^2}{d_{i\leftrightarrow\bullet}^2}\right]\right. \\ \left. \quad - \left(\sum_{i=1}^{\mathrm{N}}\left[\frac{(x_i - x_\bullet)\cdot(y_i - y_\bullet)}{d_{i\leftrightarrow\bullet}^2}\right]\right)^2\right]\end{array}\right\}}
\end{aligned} \tag{20}$$

B. Received Signal Strength

Techniques utilizing the RSS, frequently estimate the distance with the help of the Log-normal channel model

$$\tilde{P} := \tilde{P}_{RX}/dBm = A - 10\cdot\eta\cdot\log_{10}\left(\frac{d}{d_0}\right) + \tilde{N}\ ;\ \tilde{N}\sim\mathcal{N}\left(0,\sigma_{\mathrm{R}}^2\right) \tag{21}$$

Below, we derive the CRLB for these approaches. Due to the underlying Log-normal distribution, the received signal strength $\tilde{P}_{i\leftrightarrow\bullet}$ on the MS caused by a signal from BS i complies to a Gaussian distribution

$$\tilde{P}_{i\leftrightarrow\bullet} \sim \mathcal{N}\left(A_i - 10\cdot\eta_i\cdot\log_{10}\left(\frac{d_{i\leftrightarrow\bullet}}{d_0}\right), \sigma_{\mathrm{R,i}}^2\right) \tag{22}$$

where $d_{i\leftrightarrow\bullet}$ is defined as before. Without loss of generality, we assume that A_i, η_i und $\sigma_{\mathrm{R,i}}$ are identical for all BS, thus we omit index i. Hence, the conditional p.d.f. reads

$$\begin{aligned}
&f(\tilde{P}_{i\leftrightarrow\bullet}|x_\bullet, y_\bullet) \\
&= \frac{1}{\sqrt{2\pi}\sigma_{\mathrm{R}}}\exp\left(\frac{-\left[\tilde{P}_{i\leftrightarrow\bullet} - \left\{A - 10\eta\cdot\log_{10}\left(\frac{d_{i\leftrightarrow\bullet}}{d_0}\right)\right\}\right]^2}{2\sigma_{\mathrm{R}}^2}\right)
\end{aligned} \tag{23}$$

Assuming stochastically independent measurements to the N BS, we can write the joint p.d.f. with the help of the vector $\tilde{\boldsymbol{P}} = (\tilde{P}_{1\leftrightarrow\bullet}, \ldots, \tilde{P}_{N\leftrightarrow\bullet})^T$:

$$f(\tilde{\boldsymbol{P}}|x_\bullet, y_\bullet) = \prod_{i=1}^{\mathrm{N}} f(\tilde{P}_{i\leftrightarrow\bullet}|x_\bullet, y_\bullet) \tag{24}$$

Hence, the logarithmic joint p.d.f $l(\tilde{\boldsymbol{P}}|x_\bullet, y_\bullet)$ becomes

$$l(\tilde{\boldsymbol{P}}|x_\bullet, y_\bullet) := \ln\left(f(\tilde{\boldsymbol{P}}|x_\bullet, y_\bullet)\right) \tag{25}$$

A similar derivation as in the case of ToA can be performed to obtain [11]:

$$F_{x_\bullet x_\bullet} = -\mathbb{E}\left[\frac{\partial^2 l(\tilde{\boldsymbol{t}}|x_\bullet, y_\bullet)}{\partial x_\bullet^2}\right] = \mathrm{K_R}\sum_{i=1}^{\mathrm{N}}\left(\frac{(x_i - x_\bullet)^2}{d_{i\leftrightarrow\bullet}^4}\right) \tag{26}$$

$$F_{y_\bullet y_\bullet} = -\mathbb{E}\left[\frac{\partial^2 l(\tilde{\boldsymbol{t}}|x_\bullet, y_\bullet)}{\partial y_\bullet^2}\right] = \mathrm{K_R}\sum_{i=1}^{\mathrm{N}}\left(\frac{(y_i - y_\bullet)^2}{d_{i\leftrightarrow\bullet}^4}\right) \tag{27}$$

$$F_{x_\bullet y_\bullet} = -\mathbb{E}\left[\frac{\partial^2 l(\tilde{\boldsymbol{t}}|x_\bullet, y_\bullet)}{\partial y_\bullet \partial x_\bullet}\right] = \mathrm{K_R}\sum_{i=1}^{\mathrm{N}}\left(\frac{(x_i - x_\bullet)(y_i - y_\bullet)}{d_{i\leftrightarrow\bullet}^4}\right) \tag{28}$$

where we have set

$$\mathrm{K_R} = \left[\frac{100\eta^2}{\sigma_{\mathrm{R}}^2\cdot(\ln(10))^2}\right] \tag{29}$$

And finally we get the CRLB

$$\begin{aligned}
&\mathbb{E}\left[({}^{E}\tilde{x}_\bullet - x_\bullet)^2 + ({}^{E}\tilde{y}_\bullet - y_\bullet)^2\right] \\
&\geq \frac{\mathrm{K_R}^{-1}\left\{\sum_{i=1}^{\mathrm{N}}\left(\frac{(x_i - x_\bullet)^2}{d_{i\leftrightarrow\bullet}^4}\right) + \sum_{i=1}^{\mathrm{N}}\left(\frac{(x_i - x_\bullet)^2}{d_{i\leftrightarrow\bullet}^4}\right)\right\}}{\sum_{i=1}^{\mathrm{N}}\left(\frac{(x_i - x_\bullet)^2}{d_{i\leftrightarrow\bullet}^4}\right)\cdot\sum_{i=1}^{\mathrm{N}}\left(\frac{(x_i - x_\bullet)^2}{d_{i\leftrightarrow\bullet}^4}\right) - \left[\sum_{i=1}^{\mathrm{N}}\left(\frac{(x_i - x_\bullet)(y_i - y_\bullet)}{d_{i\leftrightarrow\bullet}^4}\right)\right]^2}
\end{aligned} \tag{30}$$

IV. Hybrid ToA/RSS

In a last step, we derive the CRLB for the combined system, which uses a combination of $\mathrm{N_T}$ ToA and $\mathrm{N_R}$ RSS readings. The individual p.d.f. from eq. (4) and (5) as well as from eq. (23) and (24) are used to form the joint p.d.f., where again stochastic independence is assumed

$$f(\tilde{\boldsymbol{t}}, \tilde{\boldsymbol{P}}|x_\bullet, y_\bullet) = \left[\prod_{i=1}^{\mathrm{N_T}} f(\tilde{t}_{i\leftrightarrow\bullet}|x_\bullet, y_\bullet)\right]\cdot\left[\prod_{i=1}^{\mathrm{N_R}} f(\tilde{P}_{i\leftrightarrow\bullet}|x_\bullet, y_\bullet)\right] \tag{31}$$

Since the logarithm of a product is equal to the sum of the individual logarithms of the factors, the logarithmic p.d.f. reads

$$l(\tilde{\boldsymbol{t}}, \tilde{\boldsymbol{P}}|x_\bullet, y_\bullet) := \ln\left(f(\tilde{\boldsymbol{t}}, \tilde{\boldsymbol{P}}|x_\bullet, y_\bullet)\right) = l(\tilde{\boldsymbol{t}}|x_\bullet, y_\bullet) + l(\tilde{\boldsymbol{P}}|x_\bullet, y_\bullet) \tag{32}$$

Thus, we determine the elements of the Fisher information matrix as the sum of the elements for ToA and RSS. In doing so, we finally obtain the CRLB of the hybrid system

$$\begin{aligned}
&\mathbb{E}\left[({}^{E}\tilde{x}_\bullet - x_\bullet)^2 + ({}^{E}\tilde{y}_\bullet - y_\bullet)^2\right] \\
&\geq \frac{\left\{\begin{array}{l}\mathrm{K_S}\sum_{i=1}^{\mathrm{N_T}}\left[\frac{(x_i - x_\bullet)^2}{d_{i\leftrightarrow\bullet}^2}\right] + \mathrm{K_R}\sum_{i=1}^{\mathrm{N_R}}\left(\frac{(x_i - x_\bullet)^2}{d_{i\leftrightarrow\bullet}^4}\right) + \\ \mathrm{K_S}\sum_{i=1}^{\mathrm{N_T}}\left[\frac{(y_i - y_\bullet)^2}{d_{i\leftrightarrow\bullet}^2}\right] + \mathrm{K_R}\sum_{i=1}^{\mathrm{N_R}}\left(\frac{(y_i - y_\bullet)^2}{d_{i\leftrightarrow\bullet}^4}\right)\end{array}\right\}}{\left\{\begin{array}{l}\left\{\mathrm{K_S}\sum_{i=1}^{\mathrm{N_T}}\left[\frac{(x_i - x_\bullet)^2}{d_{i\leftrightarrow\bullet}^2}\right] + \mathrm{K_R}\sum_{i=1}^{\mathrm{N_R}}\left(\frac{(x_i - x_\bullet)^2}{d_{i\leftrightarrow\bullet}^4}\right)\right\}\cdot \\ \left\{\mathrm{K_S}\sum_{i=1}^{\mathrm{N_T}}\left[\frac{(y_i - y_\bullet)^2}{d_{i\leftrightarrow\bullet}^2}\right] + \mathrm{K_R}\sum_{i=1}^{\mathrm{N_R}}\left(\frac{(y_i - y_\bullet)^2}{d_{i\leftrightarrow\bullet}^4}\right)\right\} - \\ \left\{\mathrm{K_S}\sum_{i=1}^{\mathrm{N_T}}\left[\frac{(x_i - x_\bullet)(y_i - y_\bullet)}{d_{i\leftrightarrow\bullet}^2}\right] + \mathrm{K_R}\sum_{i=1}^{\mathrm{N_R}}\left(\frac{(x_i - x_\bullet)(y_i - y_\bullet)}{d_{i\leftrightarrow\bullet}^4}\right)\right\}^2\end{array}\right\}}
\end{aligned} \tag{33}$$

V. Evaluations

In this section, we compare the theoretical CRLB with the help of evaluations. As a basis, we choose a scenario of size $10\,\mathrm{m}\times 10\,\mathrm{m}$. For localization, we employ four BS, which are put into the corners. Characteristic values are selected for the parameters, i.e. $(\mathrm{c}\cdot\sigma_{\mathrm{T}}) = 1.8\,m$ [12], $\sigma_{\mathrm{R}}^2 = 9$ and $\eta = 2.5$ [1], [13], [14] (σ_{R}^2 and η are unitless).

The figures 1a and 1b illustrate the bounds for ToA and RSS over the $10\,\mathrm{m}\times 10\,\mathrm{m}$ scenario. As presumed, more

https://doi.org/10.24355/dbbs.084-201807191218-1

accurate results can be expected for ToA, since the CRLB for ToA is below the CLRB for RSS for all points in the scenario.

In figure 1c the underlying ToA measurements are extended with regards to incorporating the four additional readings of the RSS. As already mentioned, these are determined in most cases anyway, thus no additional hardware is necessary. The evaluations reveal, that the CRLB of ToA/RSS is approximately half of ToA, for our selected parameter values, which reflect a typical use case. Therefore, a considerable accuracy improvement is expected by incorporating these RSS readings.

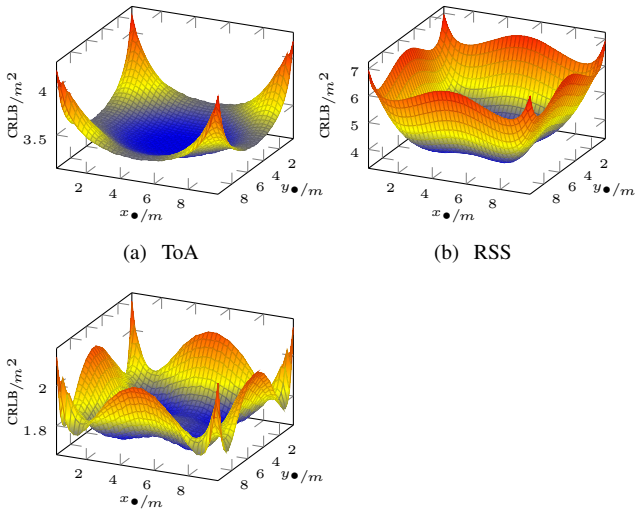

(a) ToA (b) RSS

(c) ToA/RSS

Fig. 1. CRLB for ToA, RSS and ToA/RSS

VI. Conclusion and Future Work

This paper determined the theoretical bounds for any unbiased estimator for common positioning techniques. As expected, RSS localization is inferior compared to using ToA. Our findings were supported by evaluations, where typical associated parameter values were selected. In a further step, the CRLB for the combined ToA/RSS variant was derived. Comparing all three approaches, the evaluation demonstrate that the CRLB for the hybrid technique is approximately half of the CRLB for ToA. In summary, these theoretical findings reveal that the additional application of RSS readings in a ToA system can lead to considerable performance improvements.

Acknowledgment

The research leading to these results has received funding from the European Communitys Seventh Framework Programme (FP7/2007-2013) under grant agreement ICT-FP7-611526 (MAGELLAN).

References

[1] P. Tarrio, A. M. Bernardos, and J. R. Casar, "Weighted least squares techniques for improved received signal strength based localization," *Sensors 2011*, pp. 8569–8592, 2011. DOI: 10.3390/s110908569.

[2] Z. Jianyong, L. Haiyong, C. Zili, and L. Zhaohui, "Rssi based bluetooth low energy indoor positioning," in *Int. Conf. on Indoor Positioning and Indoor Navigation (IPIN)*, Busan, South Korea: IEEE, 2014, pp. 8569–8592. DOI: 10.1109/IPIN.2014.7275525.

[3] T. Alhmiedat and S. H. Yang, "Tracking multiple mobile targets based on zigbee standard," in *35th Annual Conference of the IEEE Industrial Electronics Society*, Porto, Portugal: IEEE, 2009, pp. 2726–2731. DOI: 10.1109/IECON.2009.5415426.

[4] P. Hillmann, L. Stiemert, G. Dreo, and O. Rose, "On the path to high precise ip geolocation: A self-optimizing model," *Int. Journal of Intelligent Computing Research (IJICR)*, 2016.

[5] N. Joram, B. Al-Qudsi, J. Wagner, A. Strobel, and F. Ellinger, "Design of a multi-band fmcw radar module," in *Proc. of 10th Workshop on Positioning, Navigation and Commun. (WPNC'13)*, Dresden, Germany: IEEE, 2013, pp. 1–6. DOI: 10.1109/WPNC.2013.6533260.

[6] M. Gunia, F. Protze, N. Joram, and F. Ellinger, "Setting up an ultra-wideband positioning system using off-the-shelf components," in *Proc. of 13th Workshop on Positioning, Navigation and Commun. (WPNC'16)*, Bremen, Germany: IEEE, 2016, pp. 1–6. DOI: 10.1109/WPNC.2016.7822860.

[7] M. Gunia, A. Zinke, N. Joram, and F. Ellinger, "Setting up a phase-based positioning system using off-the-shelf components," in *Proc. of 14th Workshop on Positioning, Navigation and Commun. (WPNC'17)*, Bremen, Germany: IEEE, 2017, pp. 1–6. DOI: 10.1109/WPNC.2017.8250065.

[8] A. M. Mood, *Introduction to the Theory of Statistics*. McGraw-Hill, 1950.

[9] K. Burg, H. Haf, and F. Wille, *Höhere Mathematik für Ingenieure Band II: Lineare Algebra: 2*, 4th ed. Teubner-Ingenieurmathematik, 2002.

[10] K. Tong, X. Wang, A. Khabbazibasmenj, and A. Dounavis, "Optimum reference node deployment for toa-based localization," in *2015 IEEE International Conference on Communications (ICC)*, Jun. 2015, pp. 3252–3256. DOI: 10.1109/ICC.2015.7248825.

[11] Q. Li, W. Li, W. Sun, J. Li, and Z. Liu, "Cramér-rao bound analysis of wi-fi indoor localization using fingerprint and assistant nodes," in *Proc. of 86th Vehicular Technol. Conf. (VTC-Fall)*, Toronto, ON, Canada: IEEE, 2017, pp. 1–5. DOI: 10.1109/VTCFall.2017.8288250.

[12] N. Patwari, A. O. Hero III, M. Perkins, N. Correal, and R. J. O'Dea, "Relative location estimation in wireless sensor networks," *IEEE Trans. on Signal Processing*, pp. 2137–2148, 2003. DOI: 10.1109/TSP.2003.814469.

[13] A. M. Bernardos, J. R. Casar, and P. Tarrio, "Real time calibration for rss indoor positioning systems," in *International Conference on Indoor Positioning and Indoor Navigation (IPIN)*, IEEE, 2010, pp. 1–7. DOI: 10.1109/IPIN.2010.5648231.

[14] N. Patwari and A. O. Hero III, "Using proximity and quantized rss for sensor localization in wireless networks," *Proc. of 2nd ACM int. conf. on Wireless sensor networks and applications (WSNA 03)*, pp. 20–29, 2003. DOI: 10.1145/941350.941354.

https://doi.org/10.24355/dbbs.084-201807191218-1

Comparison of Antenna Types and Frequency Bands for Radio-based Device-free Localization

Marco Cimdins* and Horst Hellbrück*†
* Luebeck University of Applied Sciences, Germany
Department of Electrical Engineering and Computer Science
Email: marco.cimdins, hellbrueck@fh-luebeck.de
† University of Luebeck, Germany, Institute of Telematics

***Abstract*—Radio-based device-free localization systems measure effects on radio signals e.g. signal strength variations to locate objects or persons in a target area. Such systems detect and track persons that do not participate in the localization process. Models for calculating the radio signal propagation are key for the performance in device-free localization systems. Received signal strength (RSS) is simple to measure. However, it is susceptible to changes in the environment and multipath propagation. In this paper, we compare PCB antennas to a circularly polarized cloverleaf antenna and measurements in the 2.4 GHz with measurements to the 868 MHz ISM band. We investigate especially if a circularly polarized cloverleaf antenna is resilient against multipath propagation. Our preliminary results demonstrate that our model is suitable to the 868 MHz band and the use of the 868 MHz band increases the area where a person affects the RSS. The use of a circularly polarized cloverleaf antenna does not help to avoid multipath propagation.**

***Index Terms*—device-free localization, RSS models, cloverleaf antenna**

I. Introduction and Related Work

Device-free localization systems detect and track persons that do not participate in the localization process by measuring ambient signals such as RSS. That makes those systems viable for a range of applications like intrusion detection, elderly care, and smart-homes as wireless infrastructure is pervasive in our daily life and RSS measurements are performed during packet reception. Device-free localization systems are a research area for more than one decade [1]. Recent systems are able to detect and track multiple persons [2], [3], however, those system requires the use of intensive training phases.

Modeling received signal strength (RSS) is key for the design of device-free localization systems. Models enable simulation of the RSS for each wireless link, i.e. transmitter and receiver pair and the position of an obstacle such as a person. There are different approaches to model the RSS: Models based on reflection at the person are e.g. described in [4], [5]. Diffraction models assume that the planar wavefront that is obstructed by a person creates Huygens' sources at the borders, which results in a change of the RSS at the receiver [6]. In addition, there are models that describe the fade level as a measure of the existence of multipath based on the idle RSS [7].

In this paper, we investigate whether a change of the antenna or the frequency band helps in a broader coverage area of the wireless links and a more robust behavior of the RSS against multipath propagation. In addition to our measurements, we evaluate our proposed radio propagation model with a varying wavelength λ [6].

The rest of this paper is structured as follows: Section II describes the diffraction-based radio frequency propagation model. In Section III, we describe our implementation, including the system setup, the antennas, and the hardware platform. We evaluate the results of our measurements and simulations in Section IV. Finally, we conclude the results and give an outlook for future work in Section V.

II. Radio Frequency Propagation Model

In this section, we introduce our propagation model that is used to calculate the RSS at the receiver, given the position of the transmitter T_x, receiver R_x and the position P and diameter b of the person. The setup is shown in Figure 1

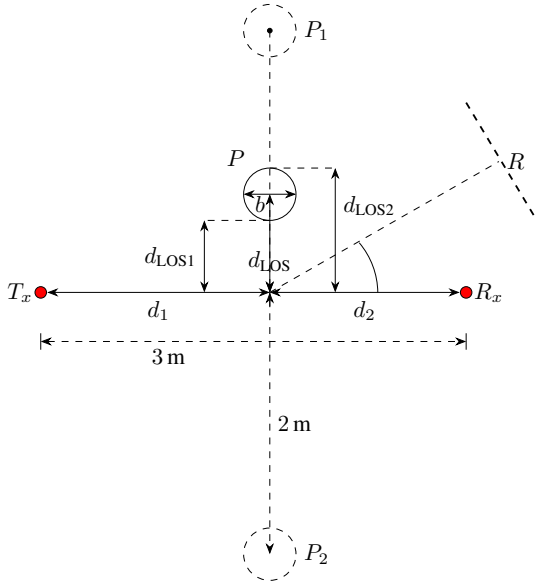

Fig. 1: Description of the geometry and the setup.

Based on the geometry of the setup, we calculate the Fresnel diffraction parameter v

$$v = d_{\text{LOS}} \sqrt{\frac{2(d_1 + d_2)}{\lambda d_1 d_2}}, \tag{1}$$

https://doi.org/10.24355/dbbs.084-201807191218-1

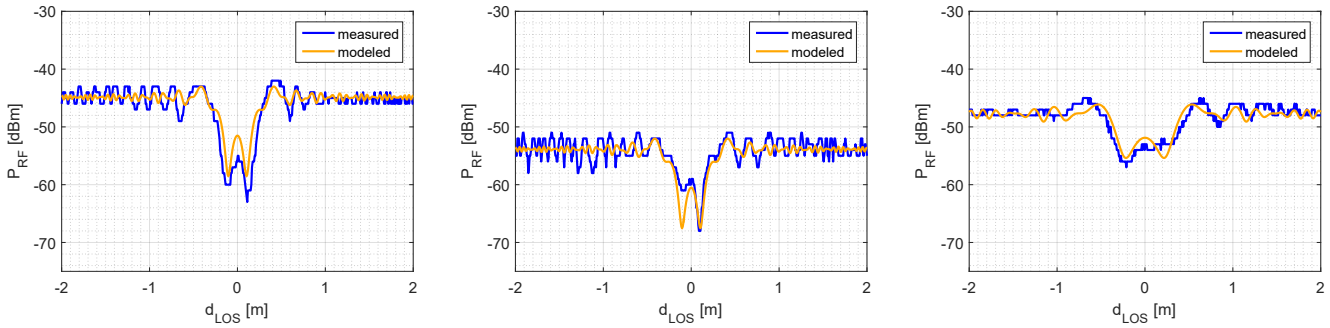

(a) 2.4 GHz with external PCB antenna. (b) 2.4 GHz with external cloverleaf antenna. (c) 868 MHz with internal PCB antenna.

Fig. 2: Exemplary results. Line in blue color is a measurement. Line in yellow color is the outcome of the model. A Person moves with constant velocity from d_{LOS} -2 to 2 m.

where d_{LOS} is the distance between the link and the position of the person P, d_1 the distance from the transmitter to the intersection of the LOS, and d_2 the distance from the receiver to the intersection of the LOS [8]. λ is the wavelength of the signal. With v we are able to calculate the complex Fresnel integral $F(v)$ that describes the change of the signal strength, relative to the free-space, caused by an obstacle spanning from $-\infty$ to d_{LOS}.

$$F(v) = \frac{1+j}{2}\left[\left(\frac{1}{2} - C(v)\right) - j\left(\frac{1}{2} - S(v)\right)\right], \quad (2)$$

$C(v)$ is the Fresnel cosine and $S(v)$ is the Fresnel sine, which can be solved numerically. Diffraction occurs above and below the boundaries of the person indicated by the diameter b, resulting in $v_1 = v(d_{\text{LOS1}})$ and $v_2 = v(-d_{\text{LOS2}})$. The superposition of the Huygens' sources is $F(v_1, v_2) = F(v_1) + F(v_2)$. $F(v_1, v_2)$ models the change of the RSS due to the presence of the person. A more detailed derivation can be found in [6].

III. Implementation

In this section, we describe the setup and hardware that is used for measurements.

We use two sets of hardware for our evaluation. For the 2.4 GHz measurements on IEEE 802.15.4 channel 25, we deploy two Texas Instruments CC2650 Launchpads that are equipped with an external inverted F PCB antenna or a cloverleaf antenna. In addition, we employ two Texas Instruments CC1350 Launchpads for measurements with the built-in PCB antenna in the 868 MHz ISM band. The devices run Contiki-NG 4.1 OS with a nullnet application that periodically broadcast a message. One device acts as a receiver and the logs the RSS value together with its timestamp and sends the data via serial interface to a PC for offline processing. The sampling interval of the sensors is approx. 15 ms.

Figure 1 shows the dimensions of the testbed. The transmitter and receiver are placed 3 m apart at a height of 1.4 m, reassembling a situation where a person walks passes the LOS of a wireless link. The person (1.95 m, 85 kg) walks with a constant speed from a distance of 4 m from P_1 to P_2, crossing the line-of-sight (LOS) of the link in the middle. For the simulation, the diameter b of the person is set to 0.35 m.

TABLE I: Measurement results for the different setups.

	2.4 GHz PCB	2.4 GHz Clover	868 MHz PCB
μ_e [dB]	-0.3	0.29	-0.32
σ_e [dB]	1.62	1.77	1.68
r	0.91	0.8	0.9

IV. Measurement and Evaluation

In this section, we evaluate the measurements in three different hardware setups. To avoid multipath effects, we performed the measurements in an outdoor environment. Figure 2 shows exemplary results for the outdoor measurements. Figure 2a and Figure 2b show the measurement and the output of our model for the external PCB and cloverleaf antenna at 2.4 GHz. Figure 2c shows the measurement and the model for 868 MHz. By visual inspection, the model fits well with the measurements. For a qualitative comparison, we calculate the mean error μ_e, the standard deviation error σ_e, and the correlation coefficient r of the difference $\Delta\text{RSS} = A - B$, where $A = \text{RSS}_{\text{measured}}$ and $B = \text{RSS}_{\text{model}}$.

$$\mu_e = \frac{1}{N}\sum_{i=1}^{N} \Delta\text{RSS}_i. \quad (3)$$

$$\sigma_e = \sqrt{\frac{1}{N-1}\sum_{i=1}^{N} |\Delta\text{RSS}_i - \mu|^2}. \quad (4)$$

$$r(A,B) = \frac{1}{N-1}\sum_{i=1}^{N}\left(\frac{\overline{A_i - \mu_A}}{\sigma_A}\right)\left(\frac{B_i - \mu_B}{\sigma_B}\right). \quad (5)$$

Table I shows the results for μ_e, σ_e, and r for every setup as the average of eight measurement runs. The correlation r between the model and the measurements are high, the mean error is close to 0 dB. The standard deviation is around 1.6 dB, which is due to problems at the peaks of the measurements and at the borders. The results for the outdoor measurement show that we are able to model RSS for different frequencies.

https://doi.org/10.24355/dbbs.084-201807191218-1

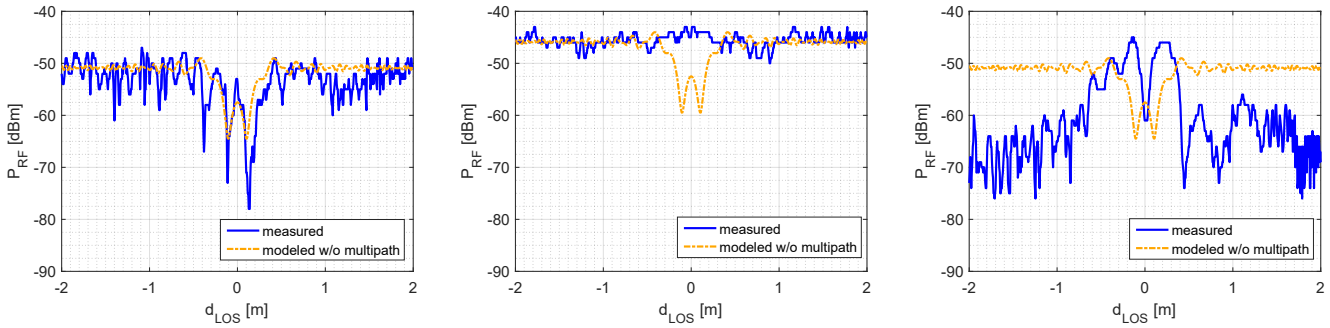

(a) Indoor w/o additional reflections.

(b) Indoor w/o additional reflections, different antenna orientation.

(c) Outdoor w/ additional reflections.

Fig. 3: Exemplary results. Line in blue color is a measurement. Person moves from d_{LOS} -2 to 2 m.

In the next step, we investigate the resilience of the cloverleaf antenna against multipath propagation. Therefore, we measured the RSS in three different environments, in addition to the outdoor scenario. a) Indoor w/o additional reflections. b) Indoor w/o additional reflections, different antenna orientation. c) Outdoor with reflections.

In an indoor environment, multipath propagation occurs, due to reflection on walls, floor, and ceilings. To create a well-defined reflection in an outside environment, we placed an obstacle at the point R as shown in Figure 1, we moved it by a few centimeters until the minimum of the RSS was measured, i.e. destructive interference occurs. Figure 3 shows exemplary results for the cloverleaf antenna.

We omit measurements of PCB antennas as we expect susceptibility to multipath. When the cloverleaf antenna is resilient against multipath, we expect that the indoor measurements do not change significantly from the outside ones (see the yellow dashed curve, which is the model without multipath propagation). In addition, we expect that destructive interference does not occur. Destructive interference reduces RSS values by approx. 20 dB compared to the free-space case.

Figure 3a shows results of an indoor measurement. The RSS value fluctuates more than in the outdoor scenario, i.e. there is multipath propagation present. Figure 3b shows results where the antenna orientation of one sensor was shifted by approx. $90°$. The measured RSS value fluctuates around a mean value, even though a person walks through the line of sight. As there is only a little change in the RSS due to a person, this Tx-Rx combination will not provide suitable measurements for a device-free localization system. Figure 3c shows an outdoor measurement and a reflection that created destructive interference. The mean of the RSS value is approx. 20 dB lower than without multipath propagation.

Based on those observations, we conclude that a cloverleaf antenna does not offer added value in terms of resilience against multipath propagation.

V. Conclusion and Future Work

In this paper, we compared three different setups and the result of our propagation model for the use in device-free localization systems. In the 2.4 GHz ISM band, we compared the externally mounted PCB and a circularly polarized cloverleaf antenna. In addition, we measured RSS values in the 868 MHz ISM band. Our model is able to calculate the RSS for measurements in the 868 MHz band. Changing the frequency and therefore the wavelength results in a change of the area, where a person is effectively changing the RSS. Our measurements show that the cloverleaf antenna is not resilient against multipath propagation as we expected. In the future, we will investigate how measurements in the 868 MHz or in the 2.4 GHz ISM-band will affect the performance and determine the best position and antenna setup for the device-free localization system.

Acknowledgments

This publication is a result of the research work of the Center of Excellence CoSA in projects RosiE (BMWi FKZ ZF4186102ED6). Horst Hellbrück is adjunct professor at the Institute of Telematics of University of Lübeck.

References

[1] S. Palipana, B. Pietropaoli, and D. Pesch, "Recent advances in RF-based passive device-free localisation for indoor applications," *Ad Hoc Networks*, 2017.

[2] C. Xu, B. Firner, R. S. Moore, Y. Zhang, W. Trappe, R. Howard, F. Zhang, and N. An, "SCPL: Indoor Device-Free Multi-Subject Counting and Localization Using Radio Signal Strength," in *2013 ACM/IEEE International Conference on Information Processing in Sensor Networks (IPSN)*. IEEE, 2013.

[3] I. Sabek, M. Youssef, and A. V. Vasilakos, "ACE: An Accurate and Efficient Multi-Entity Device-Free WLAN Localization System," *IEEE Transactions on Mobile Computing*, vol. 14, no. 2, pp. 261–273, 2015.

[4] H. Yiğitler, R. Jäntti, O. Kaltiokallio, and N. Patwari, "Detector Based Radio Tomographic Imaging," *IEEE Transactions on Mobile Computing*, vol. 17, no. 1, pp. 58–71, 2018.

[5] O. Kaltiokallio, H. Yiğitler, and R. Jäntti, "A Three-State Received Signal Strength Model for Device-free Localization," *arXiv preprint arXiv:1402.7019*, 2014.

[6] M. Cimdins and H. Hellbrück, "Modeling Received Signal Strength and Multipath Propagation Effects of Moving Persons," in *2017 14th Workshop on Positioning, Navigation and Communication (WPNC)*. IEEE, 2017, pp. 1–6.

[7] O. Kaltiokallio, M. Bocca, and N. Patwari, "A Fade Level-Based Spatial Model for Radio Tomographic Imaging," *IEEE Transactions on Mobile Computing*, vol. 13, no. 6, pp. 1159–1172, 2014.

[8] K. Balman and E. Jordan, *Electromagnetic Waves and Radiating Systems*. Prentice Hall, New Jersey, 1968.

https://doi.org/10.24355/dbbs.084-201807191218-1

https://doi.org/10.24355/dbbs.084-201807191218-1

A new localization algorithm based on neural networks

Mathias Pelka*, Manfred Constapel*, Duc Tu Le Anh* and Horst Hellbrück*†
*Lübeck University of Applied Sciences, Germany
Department of Electrical Engineering and Computer Science
Email: mathias.pelka@fh-luebeck.de, manfred.constapel@fh-luebeck.de,
duc.tu.anh@stud.fh-luebeck.de, horst.hellbrueck@fh-luebeck.de
† University of Lübeck, Germany,
Institute of Telematics

***Abstract*—Indoor localization plays a major role in a wide range of applications. To determine the location of a tag, localization algorithm is required. In the past, machine learning algorithms were difficult to implement in consumer hardware, but with the advent of tensor processing units, even smartphones are capable to use artificial intelligence to solve complex problems. In this paper, we investigate a machine learning algorithm based on neural networks and compare the result to a linear least squares estimator. We design and evaluate different neural networks. Based on our observation, the neural network delivers poor performance compared to the linear least squares estimator.**

***Index Terms*—indoor localization, neural network, linear least squares.**

I. Introduction

A number of applications benefit from location information, e.g. in the industrial, medical or consumer sector. With location information, for instance, optimization in warehouses are possible. In a medical context, personal is guided directly to emergency situations. All applications require the computation of a location and different methods exists.

Precise localization is achieved using Ultra-wideband distance estimation, e.g. based on two-way ranging. Common hardware for implementation is the Decawave DW1000, a fully integrated single chip Ultra Wideband (UWB) transceiver IC, which enables precise timestamping of messages. Using those time stamps, distance estimation is possible which is in return used for location estimation.

Localization algorithms have been well investigated in the past, including linear least squares [1], Gauss-Newton iteration [2] or the Nelder-Mead algorithm [3]. In general, the accuracy and precision of a localization algorithm are in the magnitude of the measurement error [4].

Machine learning approaches have been studied in the past, e.g. Wymeersch et al. analyzed the received waveform in [5]. This approach requires analyzing the channel impulse response which is not always available. Another approach carried out by Savic et al. [6], employed kernel-based machine learning where selected channel parameters, are projected onto a nonlinear orthogonal space. Similar to the approach of Wymeersch et al. Savic et al. also employs the channel impulse response.

In the past, usage of artificial intelligence proofed resource intensive, but with the advent of new technologies, e.g. tensor processing unit (TPU), hardware specialized for machine learning [7], this is not a problem anymore. Furthermore, specialized software packages exist, to efficiently compute neural network even in resource-constrained devices [8].

In contrast to previous work and with respect to current results, we investigate neural networks to determine the location based on distance measurements.

The rest of the paper is structured as follows: Sec. II presents neural networks in general and Sec. III shows how we adapt a neural network for our problem. We present evaluation results in Sec. IV and conclude our paper in Sec. V.

II. Neural Networks

An artificial neural network (ANN) - or neural network (NN) for short - is a generic model used for prediction and classification tasks. At the minimum, it consists of one input layer and two neural layers, singly-linked from left to right: (1) input layer, (2) hidden layer, (3) output layer. Each neural layer is populated with at least one, but possibly a various number of neurons. Each neuron obtains inputs from the outputs of all neurons of the previous layer as illustrated in Fig. 1.

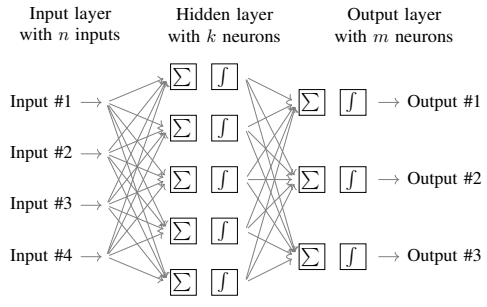

Fig. 1: Example Architecture of a 2-layer artificial neural network with $n = 4$, $k = 5$ and $m = 3$ neurons.

The inputs to a neuron are individually weighted. Subsequently, the weighted inputs are summed up, biased and fed to an activation function — usually, a step function approximated by a sigmoid function — in the figure indicated as the $\int$

https://doi.org/10.24355/dbbs.084-201807191218-1

symbol. Weights and biases of a neuron are estimated and optimized by backpropagation throughout a training phase. Backpropagation is a numerical method for minimizing the feedforward error within a neural network [9].

The number of hidden layers, as well as the number of neurons in each layer, is a design choice driven by heuristics. Since the problem of localization stated in our paper persists in a non-linear but straightforward-mapping from inputs (distances and positions) to outputs (locations), only a few hidden layers with a carefully chosen amounts of neurons are required for a decent training time while preventing overfitting. [10].

III. Neural Networks in indoor localization

The neural network in this paper consists of:

1) An input-layer with 12 input neurons, where eight neurons are used for receiving the x- and y coordinates of the reference points. The remaining four neurons are used for the distance measurements, between the tag and reference point.
2) Two hidden layers.
3) An output layer with 2 output neurons, representing the estimated x and y-coordinates.

In this configuration, the neural network supports four distance measurements. Since the tag has no inertial sensors, non-ranging or other features, e.g. IMU values, are not discussed in this paper. Nevertheless, the architecture can be easily adjusted to support more distance measurements and more output variables, e.g. to solve three-dimensional localization problems.

We also incorporate hidden layers into our neural network. To find the optimal number of hidden layers and neurons we systematically evaluate the results of different neural networks.

The weights of the neurons are randomly initialized with a standard-deviation following $2/\sqrt{x}$, where x is the number of the input values of the layer, as recommend by [9]. We use a linear activation function for the layers, which is a common choice for regression problems [9]. To evaluate the learning success of the neural network, we calculated the mean squared error between the input data and the output data. The neural network is implemented using the *TensorFlow* framework [8]. We trained the neural network over 100 000 epochs with a learning rate of $\varepsilon = 1 \cdot 10^{-5}$. The epochs describe how often we trained the neural network with our training dataset, while the learning rate describes the step size. If ε is too small, the learning takes very long, if it is too large, the network might not converge. For the training we assume a target area of 15×15 m and place four reference points at location $\mathbf{r}_1 = 2.5/2.5$, $\mathbf{r}_2 = 12.5/2.5$, $\mathbf{r}_3 = 2.5/12.5$ and $\mathbf{r}_4 = 12.5/12.5$.

One hidden layer, containing a finite number of neurons, can approximate every continuous function, [10], however, newer research [11] suggests that more hidden layers allow to reduce the number of neurons and to learn faster. Therefore we investigate different combinations of the number of hidden layers and the number of neurons in each layer to determine the optimal architecture. As of today a closed form solution for the optimal number of neurons and layers is not found [9].

We report the results of the training in Tab. I. The network is trained with four reference points, placed in the corner of a room with geometry 15×15 m. We calculate the distance to each grid point from each reference point and add noise based on a normal distribution with zero mean and $\sigma = 0.2$ m which we obtained from typical indoor distance measurements [12].

TABLE I: Mean square error (m) for learning rate $\varepsilon = 1 \cdot 10^{-5}$ and noise drawn from a normal distribution with zero mean and $\sigma = 0.2$ m.

Epochs		100	1 000	10 000	100 000	
Layers	Neurons					Time unit
1	5	34.5	11.95	1.34	0.20	0.64
1	10	53.4	14.08	0.90	0.20	0.75
1	15	49.8	7.64	0.28	0.20	0.99
2	5	68.9	8.11	0.44	0.20	0.69
2	10	92.2	2.28	0.29	0.20	1.00
2	15	9.18	0.42	0.20	0.20	1.55
3	5	33.03	6.54	0.54	0.20	0.87
3	10	60.9	1.80	0.20	0.20	1.28
3	15	10.7	1.16	0.20	0.20	2.57

Based on our investigation, we assume that after 100 000 epochs, all neural networks converge to a common mean squared error of 0.20 m. The common mean squared error indicates that neural network can't achieve better accuracy as already known algorithms. In general, the more hidden layers and the more neurons, the more training time is required for the network to converge. We normalized the runtime measurement to the neural network with 2 hidden layers and 10 neurons each. For the evaluation, we choose a network with 2 hidden layers and 10 neurons per hidden layer, which is visualized in Fig. 2. The figure shows only one input set, consisting of the x- and y-coordinate of the reference point and the distance measurement. The remaining configuration of the neural network is analogous.

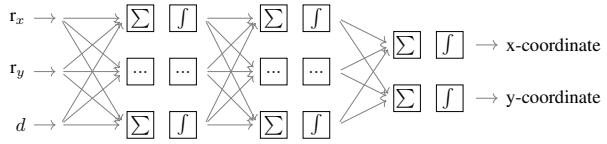

Fig. 2: Implemented neural network with 2 hidden layers. Only a subset of the input nodes is shown.

IV. Evaluation

For the evaluation, we assume the 15×15 m target area with the same location of the reference points as in the training. We divide the target area in a grid with an edge length of 0.25 m, resulting in a total of 3 600 data points. At each data point, we determine the true distances and added a Gaussian random variable with zero mean and standard deviation σ to simulate measurement inaccuracies. We then determine the location using the least squares algorithm and the neural network and calculate the Euclidean error between true location $\mathbf{r}$ and estimated location $\hat{\mathbf{r}}$. We repeated this 1 000 for each data point to retrieve reliable statistics, resulting in over 3 600 000 location calculations.

https://doi.org/10.24355/dbbs.084-201807191218-1

To evaluate the performance we calculate the mean, median, standard deviation, the interquartile range and the 95 percentile of the localization error $\mu = |\hat{\mathbf{r}} - \mathbf{r}|$ Furthermore, we determine the runtime of the neural network and linear least squares. We investigate the impact of the standard deviation for the performance. We present the results in Tab. II for least sqaures and Tab. III. We show an example visualization of the localization error of the neural network in Fig. 3. The figure shows symmetry caused by the location of the reference points.

TABLE II: Results for linear least squares for different σ.

σ (m)	0.10	0.20	0.40	1.00	2.00
mean error (m)	0.12	0.24	0.49	1.22	2.44
standard deviation (m)	0.03	0.05	0.10	0.25	0.51
median (m)	0.12	0.24	0.47	1.18	2.39
IQR (m)	0.03	0.07	0.14	0.35	0.69
95 percentile (m)	0.17	0.33	0.67	1.68	3.36

TABLE III: Results for the neural network for different σ.

σ (m)	0.10	0.20	0.40	1.00	2.00
mean error (m)	0.56	0.59	0.69	1.17	2.14
standard deviation (m)	0.31	0.30	0.26	0.21	0.27
median (m)	0.49	0.51	0.62	1.14	2.13
IQR (m)	0.38	0.36	0.29	0.23	0.35
95 percentile (m)	1.05	1.07	1.13	1.53	2.60

The mean runtime of the linear least squares is $0.08\,\text{ms}$ where the mean runtime of the neural network is $0.21\,\text{ms}$.

Based on our evaluation we conclude that linear least squares deliver better performance compared to the neural network. When the standard deviation σ increases over 1 m, the neural network delivers slightly better performance. The localization error of linear least squares increases roughly with the standard deviation, where the localization error of the neural network is at low noise levels almost constant.

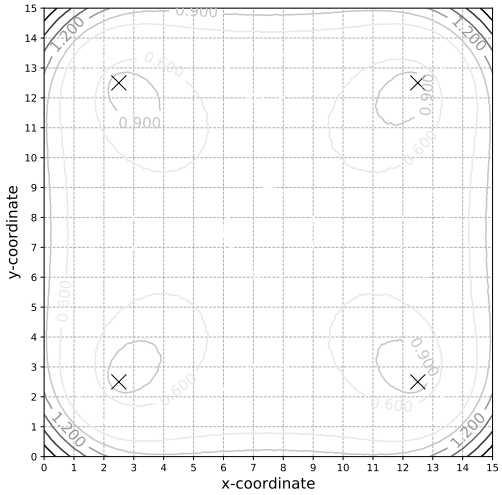

Fig. 3: Localization error of the neural network with a standard deviation of $\sigma = 0.2\,\text{m}$. The crosses indicate the location of the four reference points.

The standard deviation of consumer-of-the-shelf hardware, i.e. based on the DW1000 from Decawave achieves a distance error of below 1 m. Consequently, we do not recommend neural networks for localization estimation, as linear least squares delivers better performance.

V. Conclusion and Future Work

In this paper, we have investigated neural network for location estimation based on distance measurements. We trained a neural network using the TensorFlow framework and designed it with two hidden layers. The input layer processes the location of the reference nodes as well as the distance measurement.

The network was able to estimate the location based on our evaluation, however, the performance at low noise levels was worse compared to linear least squares. When the distance measurement was affected by larger standard deviation $\sigma > 1\,\text{m}$ of the noise component, the neural network delivers slightly better performance than linear least squares. Based on the evaluation we conclude, that our investigated neural network is not a suitable option to estimate the location.

Acknowledgments

This publication is a result of the research work of the Center of Excellence CoSA in the RosiE project (BMWi FKZ ZF4186102ED6). Horst Hellbrück is adjunct professor at the Institute of Telematics of University of Lübeck.

References

[1] H. Liu, H. Darabi, P. Banerjee, and J. Liu, "Survey of wireless indoor positioning techniques and systems," *IEEE Transactions on Systems, Man, and Cybernetics, Part C (Applications and Reviews)*, 2007.

[2] G. Shen, R. Zetik, and R. S. Thoma, "Performance comparison of toa and tdoa based location estimation algorithms in los environment," in *Positioning, Navigation and Communication, 2008. WPNC 2008. 5th Workshop on*. IEEE, 2008, pp. 71–78.

[3] M. Pelka, P. Bartmann, S. Leugner, and H. Hellbrück, "Minimizing indoor localization errors for non-line-of-sight propagation," in *International Conference on Localization and GNSS*. IEEE, 2018.

[4] Y. Zhao, X. Fan, C.-Z. Xu, and X. Li, "Er-crlb: An extended recursive cramér–rao lower bound fundamental analysis method for indoor localization systems," *IEEE Transactions on Vehicular Technology*, 2017.

[5] H. Wymeersch, S. Maranò, W. M. Gifford, and M. Z. Win, "A machine learning approach to ranging error mitigation for uwb localization," *IEEE Transactions on Communications*, 2012.

[6] V. Savic, E. G. Larsson, J. Ferrer-Coll, and P. Stenumgaard, "Kernel methods for accurate uwb-based ranging with reduced complexity," *IEEE Transactions on Wireless Communications*, 2016.

[7] TechRadar, "Google's tensor processing unit explained: this is what the future of computing looks like," 2017. [Online]. Available: https://www.techradar.com/news/computing-components/processors/google-s-tensor-processing-unit-explained-this-is-what-the-future-of-computing-looks-like-1326915

[8] M. Abadi, P. Barham, J. Chen, Z. Chen, A. Davis, J. Dean, M. Devin, S. Ghemawat, G. Irving, M. Isard *et al.*, "Tensorflow: A system for large-scale machine learning." in *OSDI*, 2016.

[9] A. Géron, *Hands-on machine learning with Scikit-Learn and TensorFlow: concepts, tools, and techniques to build intelligent systems*. " O'Reilly Media, Inc.", 2017.

[10] G. Gybenko, "Approximation by superposition of sigmoidal functions," *Mathematics of Control, Signals and Systems*, 1989.

[11] G. E. Hinton, S. Osindero, and Y.-W. Teh, "A fast learning algorithm for deep belief nets," *Neural computation*, 2006.

[12] M. Pelka, D. Amann, M. Cimdins, and H. Hellbrück, "Evaluation of time-based ranging methods: Does the choice matter?" in *14th Workshop on Positioning, Navigation and Communication*. IEEE, 2017.

https://doi.org/10.24355/dbbs.084-201807191218-1

https://doi.org/10.24355/dbbs.084-201807191218-1

Machine Learning-based Room Recognition

Zhongliang Zhao
Institute of Computer Sciences
University of Bern
Switzerland
Email: zhao@inf.unibe.ch

José Luis Carrera V.
Institute of Computer Sciences
University of Bern
Switzerland
Email: carrera@inf.unibe.ch

Torsten Braun
Institute of Computer Sciences
University of Bern
Switzerland
Email: braun@inf.unibe.ch

***Abstract*—Nowadays smartphones can collect huge amounts of data from their surroundings with the help of embedded sensors. The combination of these sensor values, such as Wi-Fi Received Signal Strengths and magnetic field measurements, is assumed to be unique in some locations, which can be used to accurately predict smartphones' indoor locations. In this work, we apply machine learning methods to derive the correlation between smartphones' locations and the received Wi-Fi signal strength and sensor values, and we have developed an Android application that is able to distinguish between rooms. Our real-world experiment results show that the Voting ensemble predictor outperforms individual machine learning algorithms and it achieves an indoor room recognition accuracy of 94% in office-like environments. This work provides a coarse-grained indoor room recognition, which can be envisioned as a basis for accurate indoor positioning.**

I. Introduction

Indoor environments provide many different ubiquitous radio signals, such as Wi-Fi, Bluetooth, magnetic field, sound, light, etc. The earth magnetic field (MF) has distortions over space due to the presence of ferromagnetic materials. These MF distortion patterns can be also used to identify indoor locations. Thereby, MF and Wi-Fi observations can be used as radio fingerprints to detect unique locations in indoor environments.

In this work, we propose to use supervised Machine Learning (ML) methods to process this large amount of collected data. By training a classifier (supervised learning algorithm such as K-Nearest-Neighbor) on the collected labeled data, rules can be extracted. Feeding in the actual live data (RSS values, magnetic field values, illuminance level, etc.) of a moving user, the trained classifier can then predict the user's location in a coarse-grained level. We propose to apply machine learning methods, both individual predictors and ensemble predictors, to solve this task due to the large amount of features that are available in indoor environments, such as Wi-Fi RSS values, magnetic field values and other sensor measurements. We expect that ensemble predictors can outperform the individual machine learning algorithms to discover patterns in the data which can then be used to differentiate between different rooms in office-like indoor environments.

II. Machine Learning-based Room Recognition

A. Algorithms

In this work, we use the following algorithms to perform the room recognition.

1) Naive Bayes (NB): classifiers are a family of simple probabilistic classifiers based on applying Bayes' theorem with strong (naive) independence assumptions between the features.

2) K-Nearest Neighbors (KNN): is a non-parametric method used for classification and regression. In both cases, the input consists of the k closest training examples in the feature space.

3) Support Vector Machine (SVM): is a supervised learning model with associated learning algorithms, which builds a model that assigns new data measurements to one category or the other, making it a non-probabilistic binary linear classifier.

4) Multilayer Perceptron (MLP): is a class of feed-forward artificial neural network. An MLP consists of at least three layers of nodes, and each node is a neuron that uses a nonlinear activation function.

5) Voting: is one of the simplest ensemble predictors, which combines the predictions from multiple individual predictors. A Voting classifier can then be used to wrap the models and average the predictions of the sub-models when asked to make predictions for new data.

B. Features

In a machine learning-based classification task, the attributes of the classes are denoted as features. Each feature is describing an aspect of the classes. In our case features are our measurements, for instance a Wi-Fi RSS value. To deliver good machine learning prediction accuracy it is very important to select the right features and to also modify certain features or even create new features out of existing features.

1) Wi-Fi RSS: Values provide the core data as they contribute the most to the performance of the ML methods. The smartphone scans the surrounding Wi-Fi access points, obtains and registers the RSS values of each access point. Wi-Fi RSS values depend on the distance between the smartphone and the Wi-Fi access points.It has a normal value of -20 dBm to -90 dBm.

https://doi.org/10.24355/dbbs.084-201807191218-1

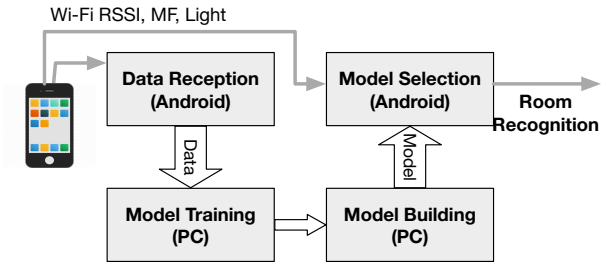

Fig. 1: The architecture of the implemented Android app.

2) Magnetic Field (MF): The device's sensors measure the magnetic field in the device's coordinate system. As the user walks around, the orientation of the device may change all the time. Therefore, we have to collect all possible values from every orientation in every point in the training phase. This would result in a huge amount of data and the training performance would be inaccurate.

3) Light: Light sensors might also be helpful to identify rooms. For instance, a room facing a window will clearly be brighter than one surrounded by walls only. As shown in Section IV, this does improve the prediction accuracy. However, these assumptions are not stable, as the illuminance level might change over time. Therefore, it is better to work with light differences instead of absolute values.

III. Experiments and Results

Figure 1 shows the system model. We made experiments in an office area of $288m^2$. We have collected 14569 data points in total, and the data collection takes around 50 minutes. With the collected data, we built models with different fingerprints data: the first one using only Wi-Fi RSSI data, the second one using Wi-Fi RSS together with MF readings, and the third one with Wi-Fi RSS, MF readings, and illuminance level readings. In our experiments, we do not need to know the locations of the Wi-Fi APs, while only the fingerprints of Wi-Fi RSSI, MF readings, and illuminance level readings are needed. We define the 9 separated areas as 9 rooms. During the online testing phase, a person holding the smartphone walks through the 9 rooms and his location is recognized in real-time based on the collected data.

A nested cross validation technique is used to optimize hyperparameters of the machine learning algorithms. The inner cross validation is to select the model with optimized hyperparameters, whereas outer cross validation is to obtain an estimation of the generalization error. For KNN, we optimized the global blend percentage ratio hyperparameter, kernel type function for SVM, number of hidden layers and neurons per layer for MLP. Based on the parameter optimization process, we established the optimal hyperparameter values for the classifiers as follows: blend percent ratio of 30% for KNN, single order polynomial kernel, $c = 1$, $\gamma = 0.0$ for SVM, and single hidden layer with 10 neurons for MLP.

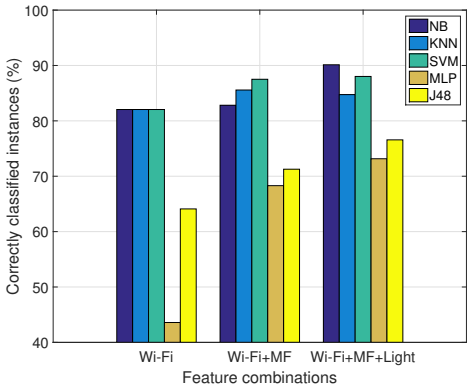

Fig. 2: Room recognition results with different features.

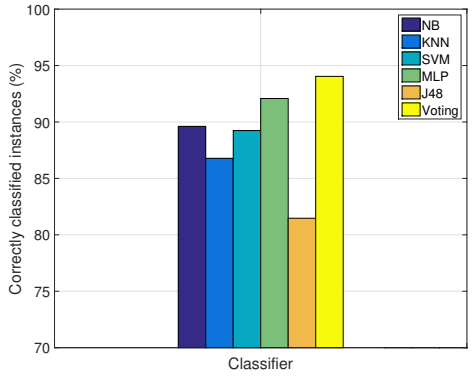

Fig. 3: Room recognition results with optimized hyperparameters.

Figure 2 shows the performance evaluation of the selected classifiers obtained with different feature combinations. The best performance is reached by the Naive Bayes classifier, which achieves 90.13% of instances correctly classified if the fingerprint is composed by Wi-Fi RSS, MF readings, and illuminance levels. By using Wi-Fi RSS, MF readings, and illuminance levels in the room landmark recognition, the accuracy is improved in all tested classifiers. Figure 3 shows the performance of the selected classifiers with the hyperparameters optimized and using Wi-Fi RSS, MF and illuminance levels. Compared to Figure 2, all the classifiers have improved performance, and MLP even reaches an accuracy of 92.08%. We also include the results of Voting, which combines the prediction results of MLP, Naive Bayes, KNN, and SVM using majority vote. It shows that Voting can reach an accuracy of 94.04%.

IV. Conclusions

This work applies machine learning methods for indoor room recognition. Results show that Voting achieves the best room recognition accuracy of 94%.

Disclaimers

The full version of this paper has been accepted for publication in the 16th International Conference on Wired/Wireless Internet Communications (IFIP WWIC), and can be found at http://dx.doi.org/10.7892/boris.116245.

https://doi.org/10.24355/dbbs.084-201807191218-1